

Design and Implementation of Torque Vectoring for the Forze Racing Car

In Collaboration with the Forze Hydrogen Racing Team

Anton Stoop



Design and Implementation of Torque Vectoring for the Forze Racing Car

In Collaboration with the Forze Hydrogen Racing Team

MASTER OF SCIENCE THESIS

For the degree of Master of Science in Mechanical Engineering at Delft
University of Technology

Anton Stoop

July 2, 2014

Faculty of Mechanical, Maritime and Materials Engineering (3mE) · Delft University of
Technology



This Thesis is done for and with the help of the Formula Zero Team Delft.



Copyright © Delft Center for Systems and Control (DCSC)
All rights reserved.



DELFT UNIVERSITY OF TECHNOLOGY
DEPARTMENT OF
DELFT CENTER FOR SYSTEMS AND CONTROL (DCSC)

The undersigned hereby certify that they have read and recommend to the Faculty of
Mechanical, Maritime and Materials Engineering (3mE) for acceptance a thesis
entitled

DESIGN AND IMPLEMENTATION OF TORQUE VECTORING FOR THE FORZE RACING
CAR

by

ANTON STOOP

in partial fulfillment of the requirements for the degree of
MASTER OF SCIENCE MECHANICAL ENGINEERING

Dated: July 2, 2014

Supervisor(s): _____

Reader(s): _____

Abstract

The Forze Hydrogen Racing team in Delft is developing the Forze VI; a hydrogen powered racing vehicle. To improve the vehicle dynamics for the Forze VI a torque vectoring approach is proposed. Torque vectoring provides vehicle stability control, for both vehicle accelerating and decelerating conditions by transmitting vectoring torque between the left and right wheels without deteriorating the longitudinal performance of the vehicle. In this thesis two different torque vectoring control algorithms will be presented. The first control algorithm is a PID and LP controller based upon a linear single-track model. The second controller is a LP controller based upon a two-track model.

Both controllers are yaw rate tracking controllers. In this thesis it is assumed that a neutral steered vehicle model provides the desired yaw rate. This neutral steered yaw rate is then imposed on the Forze VI by both controllers. The dynamics of a vehicle can be very complex. The vehicle dynamics depend upon various parameters and non-linear models. For the first controller a linear single-track model is used. This is a simplified model of the vehicle where both the front and rear tires are assumed to be one lumped mass. With this linear model a PID controller is constructed. The LP provides the left and right rear wheel torques, from the yaw moment of the controller. The LP also takes into account the friction and engine limitations. This control algorithm is only compatible with a rear wheel drive vehicle. The second controller is based upon a non-linear two-track model. In this model each wheel is separately modeled. This means that the model is more accurate but more knowledge of the vehicle parameters is needed. With this two-track model it is possible to determine the torques for all four wheels. This means that this controller will be compatible with a four wheel drive vehicle. The LP controller is a combination of the PID and LP from the previous controller. The LP controller uses the equation of motions of the two-track model to determine the torques for the left and right rear wheels, with respect to the friction and engine limits.

Both controllers show improvement of the lateral vehicle dynamics, compared to the dynamics of a vehicle with no torque vectoring. With torque vectoring the lateral acceleration is higher and therefore the velocity through corners is higher. These higher velocities through corners will translate to faster lap-times, which is the goal of this thesis. The second controller shows similar results with the first controller, but seems to have a slight more aggressive control output. Both controllers determine only the left and right rear wheel torques. The potential of four wheel drive for the second controller is not simulated, as the Forze VI is only rear wheel drive. The LP controller can in the future use it's fully potential when Forze decides to build a four wheel drive vehicle.

Table of Contents

Acknowledgements	vii
1 Introduction	1
2 Forze	3
2-1 The team	3
2-2 The car	4
2-3 Sensors	6
2-3-1 Bourns type 6002	6
2-3-2 Advanced navigation - Spatial Dual	7
2-3-3 Bosch Motorsport - ABS M4 Kit	7
2-3-4 MCS - Electronic Floor Mounted Throttle Pedal 965000	9
2-3-5 Duncan - Linear Motion Position Sensor 9600 series	9
2-4 Goal	10
3 Torque Vectoring	11
4 Simulation Setup	13
5 PI and LP Controller	17
5-1 Pre-processor	17
5-1-1 Steady-state vehicle behavior	17
5-1-2 Steady-state vehicle stability	19
5-1-3 Steering	20
5-1-4 Desired vehicle behavior	21
5-2 Yaw rate control	23
5-3 Post-processor	27

5-3-1	Slip prevention	28
5-3-2	Electrical motor model	33
5-3-3	Linear programming control	35
6	Results PI and LP Controller	39
6-1	Step response	39
6-2	Constant steer input	42
6-3	180° turn	43
6-4	Double lane change	45
6-5	Conclusion	46
7	LP Controller	49
7-1	Control algorithm	50
7-2	Vehicle modeling	53
7-2-1	Steering	54
7-2-2	Wheel velocities	54
7-2-3	Wheel slip	56
7-2-4	Friction coefficient	59
7-2-5	Lateral forces	60
7-3	Constraints	62
8	Results LP Controller	65
8-1	Step response	65
8-2	Constant steer input	68
8-3	180° turn	68
8-4	Double lane change	70
8-5	Conclusion	71
9	Conclusion	73
10	Future Work Proposals	79
10-1	More detailed modeling	79
10-1-1	Tire model	79
10-1-2	Steering model	79
10-2	Tire-Road friction model	80
10-3	More comprehensive simulations	80
10-3-1	Circuit simulation	80
10-3-2	Real-time simulation	80
10-4	Pre-processor	81
10-5	Suspension jounce measurements	81
10-6	Noise testing	81

Bibliography	83
Glossary	85
List of Acronyms	85

Acknowledgements

The thesis at the Forze Hydrogen Racing Team, is a continuation of my literature survey of torque vectoring. I would like to thank the Forze Hydrogen Racing Team for the help and guidance during the period I was working on the torque vectoring control method for the Forze VI. I would especially like to thank Niels van Duijkeren, the chief control system at Forze for all his help.

I would like to thank my supervisor Prof.dr.ir. E.G.M. Holweg for his support and guidance during my thesis at the Forze Hydrogen Racing Team. The monthly appointments were a huge contributing factor to the successful ending of this thesis. This helped me to create a good schedule. Despite his limited time at the TU Delft, there was always time that I could drop by.

Further I would like to thank Dr.ir. E.J.H. de Vries who has been my daily supervisor. Our progress meetings we had every two weeks stimulated me to stay on schedule. His sound advice, honest comments and willingness to help were invaluable. Unfortunately he left in Augustus, I wish him all the luck and he will be missed.

At last, I would like to thank Dr.ir. M. Mazo Jr. for being my next daily supervisor. Who gave me a lot of guidance and help in the final period of my thesis.

Delft, University of Technology
July 2, 2014

Anton Stoop

“Anyone who has never made a mistake has never tried anything new.”

— *Albert Einstein*

Chapter 1

Introduction

Today's vehicles are full of electronic control systems. All these control systems try to give the vehicle an ideal balance between ride comfort, response, lateral performance, stability and fuel economy. Well known vehicle stability control systems, which give the vehicle better stability and controllability are Electronic Stability Program (ESP) and Anti-lock Braking System (ABS). In this thesis another vehicle stability control system is chosen, called Torque Vectoring (TV). This vehicle stability control system is especially suited for electrical vehicles. This system has the potential to improve both the stability and the response of the vehicle without sacrificing comfort and safety.

Forze is a student team from the Delft University of Technology (TU Delft). The team specializes in building hydrogen racing vehicles. The Forze VI is designed for national circuits to compete against petrol powered racing vehicles. The goal of Forze this year is to compete in the Caterham Cup and set a lap record for hydrogen fuel cell vehicles, at the Nürburgring Nordschleife. The Forze VI will feature a lightweight bodywork with a diffuser for improved aerodynamics. It will be one of the very first sports vehicles with a fuel cell system worldwide. The Forze VI is Rear Wheel Drive (RWD) with two separate electrical motors. These two electrical motors are powered by the fuel cell and a buffer from ultracapacitors.

To improve the performance of the vehicle, torque vectoring can be used. Torque vectoring provides vehicle stability control, regardless of whether the vehicle is accelerating or decelerating by transmitting vectoring torque between the left and right wheels without deteriorating the longitudinal performance of the vehicle. Torque vectoring can therefore be used to increase the performance at all time. Because of this characteristic, torque vectoring will be used in the Forze racing vehicle to increase the overall performance.

Firstly, the Forze team and Forze VI will be introduced in Chapter 2. The specifications of the Forze VI will be presented as well as the sensors that are available for the control. The last section of this chapter will be about my role at Forze and what the goal is of this thesis. In Chapter 3, the principle of torque vectoring will be explained. Chapter

4 will show the framework of the simulation setup and which software was used. In Chapter 5, the first of two controllers will be presented. This first controller is a linear control method that consist of a Proportional Integral (PI) controller and a Linear Programming (LP) problem. The results of this controller will be shown in Chapter 6. The second controller will be presented in Chapter 7. This is a LP controller and uses non-linear vehicle and tire models. This LP controller is based on an optimization problem with dynamic constraints. In Chapter 8 the results will be presented of the LP controller. In Chapter 9 the conclusion will be given and will show the difference between the two controller. The future work proposals can be found in Chapter 10.

Chapter 2

Forze

In this chapter some insight will be given in the student team of Forze and the Forze VI. The first section will be an introduction about the team and the car. The second section will present the specifications and vehicle parameters of the Forze VI. The third section will show the specifications of the sensors used in the Forze VI. The final section will be about my role and goal in the team.

2-1 The team

Forze is a foundation that comprises about 70 students, see Figure 2-1. Most of these students study at the Delft University of Technology (TU Delft). The team is multi-disciplinary; all the faculties are represented by their students and the team is also managed by students. This year a new era for the team starts: a step into the automotive racing world. The Forze VI is designed for national circuits to compete against petrol powered racing cars. The Forze VI has six times more power than the Forze V, which entered in the Formula Student last year. The goal is to compete in the Caterham Cup and set a lap record for hydrogen fuel cell cars, at the Nürburgring Nordschleife. The car will feature a lightweight bodywork with a diffuser for improved aerodynamics. This car will be one of the very first sports cars with a fuel cell system worldwide.

Forze is considering hydrogen as one of the future solutions to power vehicles and other applications, even at home. Car manufacturers like Hyundai, Mercedes and Honda are developing fuel cell cars and are aiming to sell these cars to the public from 2015. Many European countries are investing into a hydrogen filling station network to accommodate these cars. Germany is a perfect example, this country aims for 50 hydrogen fuel station in 2015. At this moment, hydrogen fuel cell race cars are rare. Forze and Green GT are the only two parties which develop high power fuel cell race cars

at this moment. Forze is the only student team working with high power automotive fuel cells worldwide.

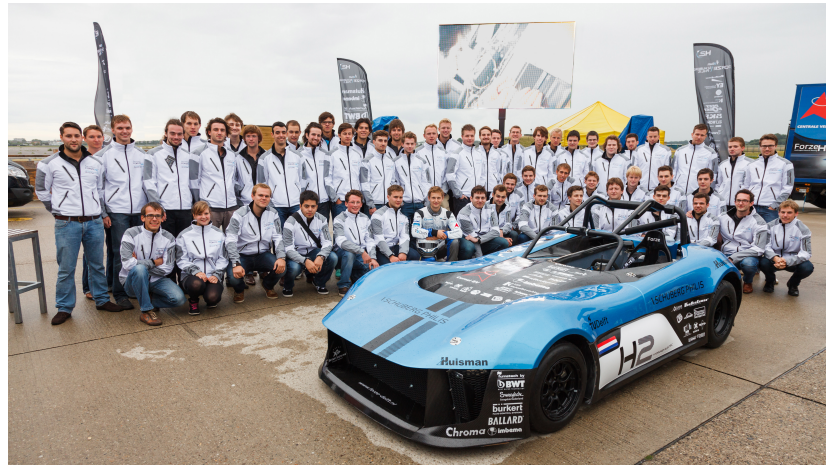


Figure 2-1: All the members of team Forze

The difference between a hydrogen and electrical car is the energy resource: A battery car stores the electric energy in a battery while a hydrogen vehicle stores energy in hydrogen. This hydrogen is converted in a fuel cell system to electric energy. This hydrogen can be filled within minutes, similar as petrol at a filling station. This means that a hydrogen fuel cell car is perfectly suitable for traveling long distance without having to recharge.

2-2 The car

The Forze VI is based on a Lotus 7 type frame. This frame was chosen such that the Forze VI could participate in the Caterham Cup. By choosing the Lotus 7 type frame it was a challenge to package the large hydrogen fuel cell into a frame which originally was designed for a relative small combustion engine. The large fuel cell provides the power together with the energy buffer. Because of the size of the frame and the fuel-cell, little room was left for other components. Therefore the majority of all the components around the fuel cell needed to be tailor made. The air system must pump 5000 liters of air through the system to provide enough oxygen to run the fuel-cell at maximum power. Many components like the motors, DC/DC converter, energy buffer, and air pump need to be cooled. To cool all these components a very large radiator is installed at the front of the vehicle. The total amount of hydrogen in the two tanks is about 3 kg. The placement of most components can be seen in Figure 2-2. In Table 2-1 the specifications of the Forze VI are listed. The acceleration time listed in the table is only achieved when the buffer is completely full, the same holds for the top speed listed in the table.

Table 2-2 shows all the vehicle parameters and Table 2-3 shows all the aerodynamic parameters of the Forze VI:

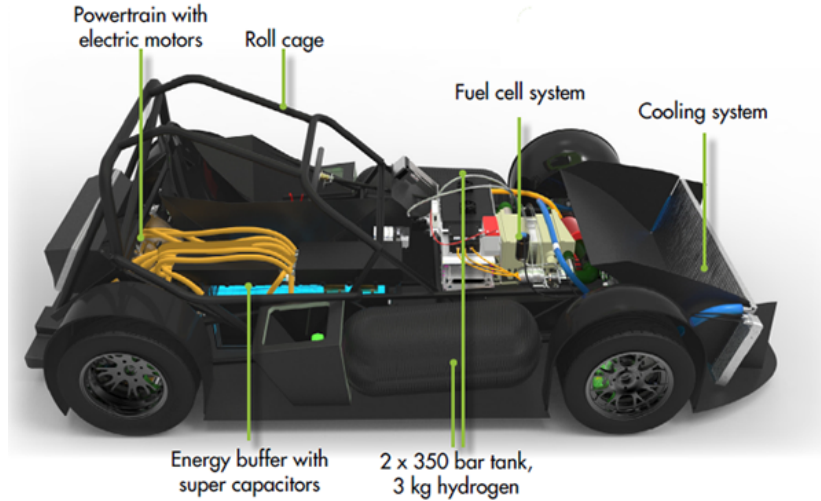


Figure 2-2: figure of the Forze VI and the placement of the components

Table 2-1: Specifications Forze VI

0 – 100 km/h	< 4 seconds
Top speed	210 km/h
Suspension	Push rod with carbon links
Fuel Cell system	Ballard FC Velocity MK1100 stack
Drive-train	2 Planetary Gears (ratio 1 : 3.66)
Motor	2 YASA400 Motors

Table 2-2: Vehicle parameters Forze VI

Parameter	Value	Units
Fuel Cell power	100/135	[kW/hp]
Boost power	190/258	[kW/hp]
Weight	790 + 120	[kg]
Front track	1500	[mm]
Rear track	1750	[mm]
Wheel base	2330	[mm]
Center of gravity front arm	1250	[mm]
Center of gravity rear arm	1080	[mm]
Roll center height front	40	[mm]
Roll center height rear	56	[mm]
Center of gravity height	335	[mm]
Static radius front tire	2778	[mm]
Static radius rear tire	2876	[mm]

Table 2-3: Aerodynamic parameters Forze VI

Parameter	Value	Units
Lift coefficient	0.46	
Drag coefficient	0.5	
Pitch coefficient($\downarrow +$)	-0.035	
Roll coefficient	0.035	
Down-force on the front	25	[%]
Center of pressure height	35	[mm]
Frontal area	1.3	[m ²]

Table 2-4: Sensors Forze VI

Measured parameter	Symbol	Sensor	Output
Throttle signal	Pedal	MCS - Electronic Floor Mounted Throttle Pedal 965000	[0 – 1]
Brake signal	Pedal	Duncan - linear motion position sensor 9600 series	[−1 – 0]
Yaw rate	$\dot{\psi}$	Advanced navigation - Spatial Dual	[rad/s]
Velocity	v_{CoG}	Advanced navigation - Spatial Dual	[m/s]
Acceleration	a_x, a_y, a_z	Advanced navigation - Spatial Dual	[m/s ²]
Side slip angle	β	Advanced navigation - Spatial Dual	[rad]
Steering wheel angle	δ_w	Bourns type 6002	[rad]
Wheel angular velocity	ω_{ij}	Bosch Motorsport - ABS M4 Kit	[rad/s]

2-3 Sensors

In this section the sensors used in the Forze VI will be presented. The control method presented in this thesis will be designed especially for the Forze VI. This means that no assumption can be made on the availability of measured data from sensors. Only the data of the sensors in the Forze VI can be used for the controller. Therefore it is important to know which sensors are available, and what the specifications are of these sensors. Table 2-4 shows all the sensors that are used in the Forze VI. This table also shows which parameter is measured by which sensor.

2-3-1 Bourns type 6002

For the steering wheel angle sensor a non-contact multiturn angle sensor type 6002 from Bourns is chosen. This sensor is based on two magneto-resistive (AMR) sensor chips; each of them converts an angle position of a permanent magnet into two analogue signals (one sine and one cosine signal). A high efficient algorithm allows for estimating the absolute angular position of a drive shaft which is connected to the device. The sensor is mounted on the steering wheel axis just before the steering rack connection. By placing the sensor close to the the rack, the error in rotation of the steering axis due to torsional effect is kept as small as possible. In Table 2-5 the data sheet of the steering sensor is presented.

Table 2-5: Steering wheel sensor data sheet

Angular position	
Range	$\pm 740^\circ$
Resolution	$\pm 0.1^\circ$
accuracy	$\pm 2^\circ$
Angular speed	
Range	$\pm 1800^\circ$
Resolution	$\pm 4^\circ$
Data & Control Interface	
CAN 2.0A	500kbits/s
Data rate	10ms

2-3-2 Advanced navigation - Spatial Dual

For the measurement of the vehicle parameters a dual Global Positioning System (GPS) antenna with an Inertial Measurement Unit (IMU) is chosen. The dual GPS antenna with IMU in de Forze VI is from Advanced Navigation and is called the Spatial Dual. The Spatial Dual is a ruggedized miniature GPS aided inertial navigation system and AHRS. It provides accurate position, velocity, acceleration, and orientations. The Spatial Dual combines temperature calibrated accelerometers, gyroscopes, magnetometers, and a pressure sensor with a dual antenna RTK GNSS receiver. The two GPS antennas are mounted in a straight line at the nose and at the rear of the vehicle. This is done to create the largest distance between the two antennas, which will increases the accuracy of the side slip angle β . The IMU is placed as close to the Center of Gravity (CoG) as possible. This is to ensure correct measurements for the yaw rate, velocity and accelerations. The data sheet is presented in Table 2-6:

2-3-3 Bosch Motorsport - ABS M4 Kit

The Bosch Motorsport ABS M4 Kit is primarily used for the ABS in the Forze VI. The Bosch Motorsport ABS M4 Kit can also be used to measure the the wheel speed of all four wheels. The Bosch Motorsport ABS M4 kit uses four wheel speed sensors with DF11 standard. To acquire the wheel speed data from the speed sensors a wheel speed signal splitter from Bosch is used. This splitter works by forwarding the sensor information to the ABS. In addition it converts the speed info into a digital signal. The wheel speed sensor of Bosch uses an encoder to measure the wheel speeds. The encoder wheel that is used has 48 teeth. The tooth/gap ratio is approx. 50% and the teeth are approx. 3 mm in height. The encoder wheel is made of a ferromagnetic material. Unfortunately Bosch still has not the data sheet with the accuracy for these measurements.

Table 2-6: Advanced navigation - Spatial Dual data sheet

Navigation	
Horizontal position accuracy	0.008 m
Horizontal position accuracy	0.015 m
Roll & pitch accuracy (static)	0.1°
Heading accuracy (static)	0.1°
Roll & pitch accuracy (dynamic)	0.15°
Heading accuracy (dynamic)	0.1°
Internal filter rate	1000 Hz
GNSS	
Update rate	20 Hz
velocity accuracy	0.007 m/s
Timing accuracy	20 ns
Acceleration limit	11 g
Accelerometers	
Range (dynamic)	2/4/16 g
Noise density	150 µg/√Hz
Non-linearity	< 0.05%
Bias stability	20 µg
scale factor stability	< 0.05%
cross axis alignment error	< 0.05°
Bandwidth	400 Hz
Gyroscopes	
Range (dynamic)	250/500/2000 °/s
Noise density	0.009 °/s/√Hz
Non-linearity	< 0.05%
Bias stability	3 °/h
scale factor stability	< 0.05%
cross axis alignment error	< 0.05°
Bandwidth	400 Hz

Table 2-7: brake sensor data sheet

Angular position	
Travel angle	22°
Angle options	30°, 35°, 45°
Return springs	2
Sensor type	Dual Analogue Hall effect sensor

Table 2-8: brake sensor data sheet

Angular position	
Total Electrical Travel	25.4 mm
Active Electrical Travel	22.8 mm
Total DC Resistance ±25%	3.4 K
Linearity Over Active Electrical Travel	±25.4%
Best Practical Linearity	±25.4%
Mechanical Travel ±0.4	25.4 mm

2-3-4 MCS - Electronic Floor Mounted Throttle Pedal 965000

For the throttle sensor an electronic floor mounted throttle pedal is used from Mobile Control Systems (MCS). The pedal used in the Forve VI is from the 965000 series. It is a heavy duty pedal, and is made from strong poly-amide. The sensor used in the pedal is a dual analogue hall effect sensor. It is possible to change the angle of the pedal in rest position. A high angle for the rest position was therefore possible. The pedal has an malfunction indicator lamp, which will be very useful while testing, and can be configured to user preference. The data sheet of the throttle pedal is presented in Table 2-7.

2-3-5 Duncan - Linear Motion Position Sensor 9600 series

For the brake sensor a linear motion position sensor is used. The linear motion position sensor is from Duncan Electronics division and is of the 9600 series. This sensor was mainly chosen because of its size. The sensor is one of the smallest from factors available, and it there fore ideal for the tight space behind the brake pedal. This potentiometer consist of an integral slider/contact assembly which assures smooth, noise-free travel over the unit's proprietary infinite resolution element to compliment sensitive systems controls. The potentiometer consist of a 3.8 mm short length terminal tab. The data sheet of the brake pedal is presented in Table 2-8. 2-5 the data sheet is presented.

2-4 Goal

My role in Forze is to design a control algorithm that determines the drive torques for each electrical motor. The Forze VI is an Rear Wheel Drive (RWD) vehicle, this means that there are only two drive torques to determine. The determination of the drive torques for the Forze VI must be done in such a way that the performance of the Forze VI increases, with respect to the performance of a 50/50 drive torque ratio. To accomplish this there is chosen to use torque vectoring. Torque vectoring is capable of changing the dynamic vehicle behavior by varying the drive torques. This means that the drive torque ratio is varying while driving and will no longer be fixed. The task at Forze is therefore to make a control algorithm that is based on torque vectoring which will increase the performance of the Forze VI. This increase of performance it measured in faster lap times.

The problem statement of this thesis is therefore as follows:

“Constructing a torque vectoring algorithm which ensures better lateral vehicle performance and faster lap times, than when no torque vectoring is used.”

To prove that torque vectoring is capable of an increase in performance, simulations will be executed which will show the difference in cornering behavior, compared with a vehicle without torque vectoring. When the simulations show that a vehicle with torque vectoring is faster through a corner and has an higher exit velocity, torque vectoring improves the cornering behavior. This improve in cornering behavior should result in faster lap times, as each corner is completed in a shorter amount of time.

Chapter 3

Torque Vectoring

Torque vectoring is one of the most important stability control systems in development today. Torque vectoring can effectively enhance the vehicle handling performance without deteriorating the longitudinal performance of the vehicle. In most situations torque vectoring is used as a stability control system, which improves the safety. This study will use torque vectoring not to improve the safety but to improve the performance. When torque vectoring is used for safety, the yaw rate will be reduced to prevent the vehicle from spinning. Torque vectoring can also be used to increase yaw acceleration. The additional yaw moment will then increase the lateral vehicle dynamics and therefore increase the vehicle cornering behavior.

Torque vectoring principle

Figure 3-1 shows a schematic top view of a vehicle. Just as the Force VI this is only a Rear Wheel Drive (RWD) vehicle. This figure shows the operation of the right-and-left torque vectoring system. The torque vectoring control system works by controlling the direction and the magnitude of the vectoring torque T_v transmitted between the left and right wheels. The driving force T_v/R acts on one wheel and the braking force $-T_v/R$ acts on the other wheel. This will generate a driving force difference indicated here as ΔD , it also generates an additional yaw moment M_z that acts on the vehicle. So when $T_v = 0$ the engine torque T_e is divided equally between the left and right wheel, a distribution of 50/50. The left-and-right torque vectoring system influences the vehicle in two ways. Firstly, the optimal distribution of driving forces expands the cornering limit. Secondly, the optimum distribution of cornering forces between front and rear wheels also expands the cornering limit.

Figure 3-2 shows the maximum friction circles of the left and right tires, the driving forces acting on both tires and the maximum cornering force. The figure shows a turn to the left. It can be seen that in this case the force circle of the left tire R_l is smaller than the force circle of the right tire R_r . This is due to the weight change of the vehicle. When taking a left turn, due to the centrifugal force, the weight increases on the outer

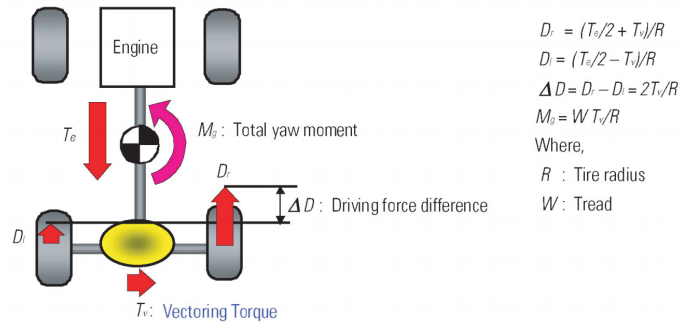


Figure 3-1: Definition of left and right torque vectoring [1]

wheels. This will increase the friction circles of the outer wheels. This results in a decrease in weight in the inner wheels. The same applies to the friction circles.

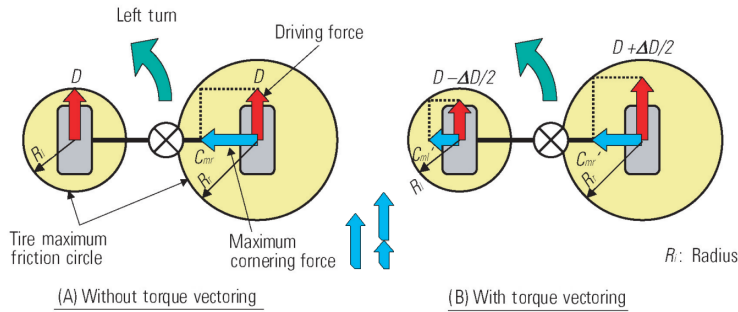


Figure 3-2: Effect of torque vectoring [1]

In case A, which is without torque vectoring, the frictional force of the left tire R_l is assumed to be equal to the driving force D . This means that the inner wheel limits the driving force for both wheels. On the right tire the same driving force D is applied. Because the driving force is smaller than the friction circle R_r only the right wheel is capable of generating the maximum cornering force C_{rr} .

In case B, which is with torque vectoring, the left tire driving force is now $D - \Delta D/2$. Due to the fact that this new driving force is smaller than the friction circle R_l , the left wheel is now capable of generating a maximum cornering force of C'_{rl} . The new driving force for the right wheel is $D + \Delta D/2$. This new driving force is still smaller than the friction circle. Therefore, the right wheel is still capable of generating a maximum cornering force of C'_{rr} . When no torque vectoring is used there is only one cornering force on the right tire C_{rr} . With torque vectoring each tire is capable of generating a cornering force C'_{rl} , C'_{rr} . The combination of the two cornering force in case B are always larger than the total cornering force in case A. This means that right-and-left torque vectoring increases the total maximum cornering force of the left and right tires.

$$C_r \leq C'_{rl} + C'_{rr} \quad (3-1)$$

Chapter 4

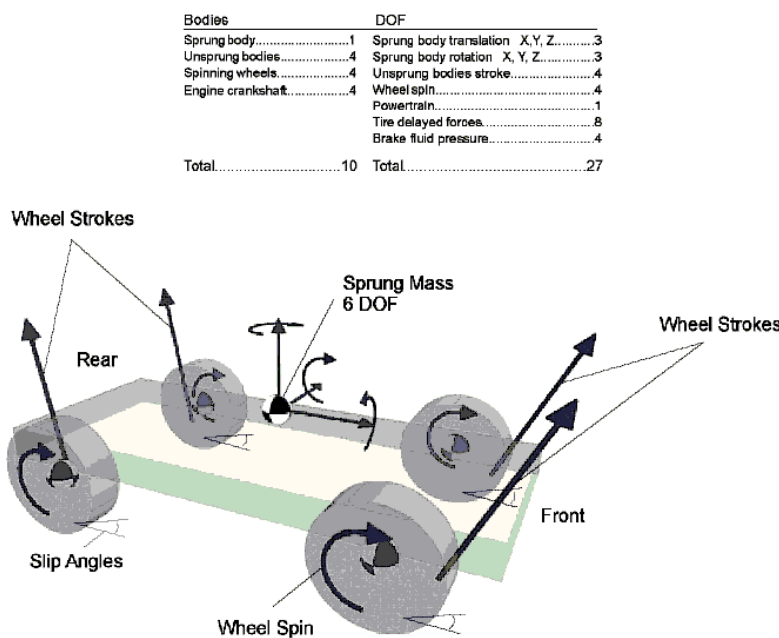
Simulation Setup

To perform the simulations a full-vehicle model in CarSim is used. CarSim consists of a central modeling engine that performs all of the mathematical processing of the vehicle dynamics, properties, input and output parameters. Around the core components an application environment is used to interact with the math model in a stand-alone application. The CarSim modeling engine can also be used by itself to integrate its simulation capabilities with other software. An example is the LabVIEW application which will be used in this thesis for the control algorithm. In this configuration only the simulation and modeling functionality is exported and integrated within LabVIEW. All vehicle properties are supplied to the model in a set of configuration files, while the model dynamic inputs and outputs are exchanged with the host application.

Figure 4-1 shows one of the models (four wheel independent suspension) used within CarSim to calculate the dynamic behavior of a vehicle. The figure shows the different bodies and forces, which are used to track the motion of the individual vehicle components and the overall frame. Individual forces such as brake pressure, acceleration, and friction with the road surface are tracked and calculated for each wheel individually. This is to determine the overall behavior of the vehicle.

Table 4-1: Import and Export channels Carsim

Import	Export
T_{rl}	β
T_{rr}	$\dot{\psi}$
	v_{CoG}
	a_x, a_y
	ω_{ij}
	δ_w
	throttle
	brake

**Figure 4-1:** Body and force diagram of the mathematical model used in CarSim for vehicle dynamics simulation

The vehicle parameter use in CarSim are from the Forze VI. This includes models of all vehicle components forces: suspension, steering, and aerodynamics. There is no drive-line modeled because the output vector of LabVIEW consist of the drive torques. The drive torques are directly send to rear wheels. See Table 4-1 for the import and export values of CarSim.

LabVIEW provides an ideal platform for evaluation applications with its deterministic run-time environment and graphical application development tools. LabVIEW is therefore used to construct the control algorithm for both controllers. The LabVIEW Real-Time module enables this control algorithm to run deterministically in a real-time environment on high performance PXI controllers. Figure 4-2 shows the top-level diagram of the interchangeable timed loop of the CarSim modeling engine. This diagram is interchangeable because it only needs the 'Carsim input' and the 'Powertrain in'

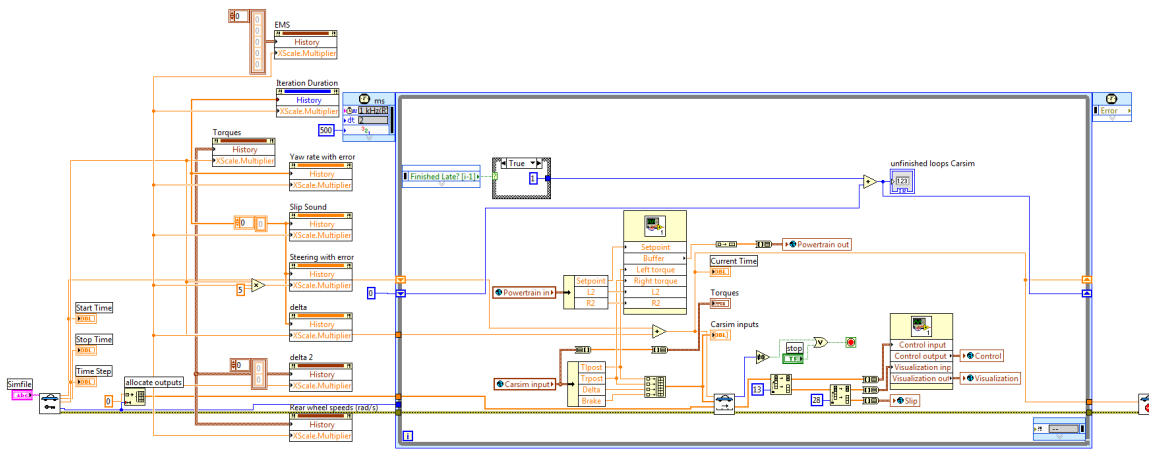


Figure 4-2: LabVIEW diagram of the interchangeable CarSim timed loop

input vectors. Both vectors come from the control algorithm in the controller timed loop diagram. By changing the diagram, the controller can be changed. This way it is easy to switch between the two different controllers. Before the main loop is started, the CarSim modeling engine is initialized and the static properties of the simulated vehicle are loaded.

Chapter 5

PI and LP Controller

For the first control method of the Forze VI, the following control setup in Figure 5-1 is chosen. In the upcoming sections each control block will be discussed in more detail. The Results of this control method will be presented in Chapter 6

5-1 Pre-processor

In this section the working of the pre-processor will be explained. In the first two sections two analyses will be presented. The first analyses will be done on the vehicle steady-state vehicle behavior, the other on the vehicle steady-state vehicle stability. The third section will present a model to determine the steering angle δ . The final section will present the model for the desired vehicle behavior.

5-1-1 Steady-state vehicle behavior

In this section, the steady state vehicle behavior of a vehicle will be investigated. There are three types of vehicle behaviors which are defined for vehicles; Over-steer, under-

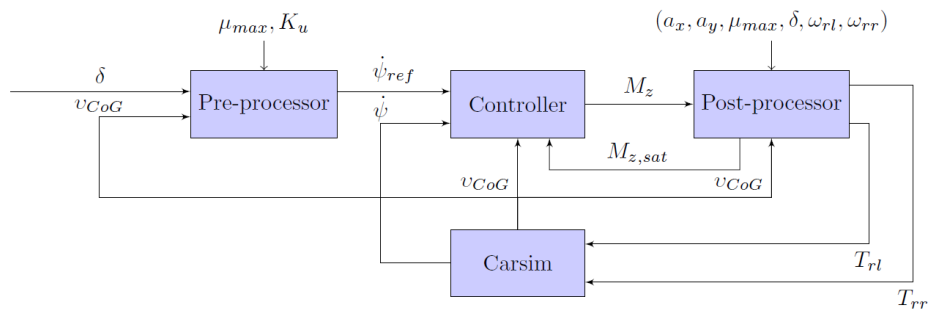


Figure 5-1: PI and LP control setup

steer and neutral-steer [2, p. 54-60]. To label these situations, an over-steer gradient is defined in equation 5-1.

$$K_u = \frac{m_f}{C_f} - \frac{m_r}{C_r} \quad (5-1)$$

Please note that the cornering stiffness used in this paper is the combined cornering stiffness of both wheels: $C_{fl} + C_{fr} = C_f$, hence no multiplication of 2 is used. This can differ from other papers.

Here, $m_r = m \frac{\ell_f}{\ell}$ which is the portion of the mass carried on the rear axis and $m_f = m \frac{\ell_f}{\ell}$ is the portion of the mass carried on the front axis. The turning radius of a vehicle for a certain velocity is also defined within the referred literature. The turning radius of a vehicle R is determined by equation 5-2. In the equation, ℓ is defined as $\ell = \ell_f + \ell_r$.

$$R = \frac{L}{\delta} + K_u \frac{v_{CoG}^2}{\delta} \quad (5-2)$$

For K_u , three situations are defined. In addition the variable α_i is also defined as the slip angle of the respective wheel. The slip angle denotes the difference in the orientation of the wheel compared to the actual velocity direction of a wheel.

- Neutral-steer

In this case the under-steer gradient is zero due to equal slip angles at the rear and front tires.

$$\frac{m_f}{C_f} = \frac{m_r}{C_r} \rightarrow K_u = 0 \rightarrow \alpha_f = \alpha_r$$

In the case of neutral steer, no change in the steering angle is required as speed is varied. The steering angle depends only on the curve radius and the wheelbase.

- Under-steer

In this case the under-steer gradient $K_u > 0$ due to a larger slip angle at the front tires compared to the rear tires.

$$\frac{m_f}{C_f} > \frac{m_r}{C_r} \rightarrow K_u > 0 \rightarrow \alpha_f > \alpha_r$$

In the case of under-steer, on a constant radius turn, the steering angle will have to increase with speed in proportion to K_u times the lateral acceleration.

- Over-steer

In this case the under-steer gradient $K_u < 0$ due to a larger slip angle at the rear tires compared to the front tires.

$$\frac{m_f}{C_f} < \frac{m_r}{C_r} \rightarrow K_u < 0 \rightarrow \alpha_f < \alpha_r$$

In the case of under-steer, on a constant radius turn, the steering angle will have to decrease with speed in proportion to K_u times the lateral acceleration.

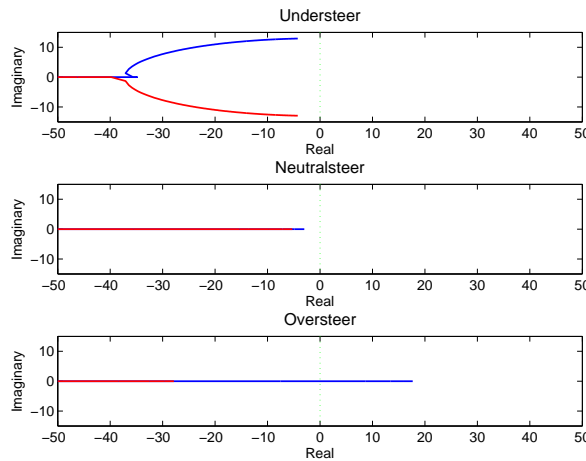


Figure 5-2: State matrix eigenvalue plot for different steady-state vehicle behavior and increasing velocity [3].

5-1-2 Steady-state vehicle stability

In this section, the stability will be evaluated for the three defined states above. Here, the state equations from 5-14 are used. The eigenvalues of the state matrix will be evaluated for the three different steering behaviors of a vehicle. Since this equation is depending on the velocity, it will be evaluated for all v_{CoG} within the achievable velocity domain of the Forze VI.

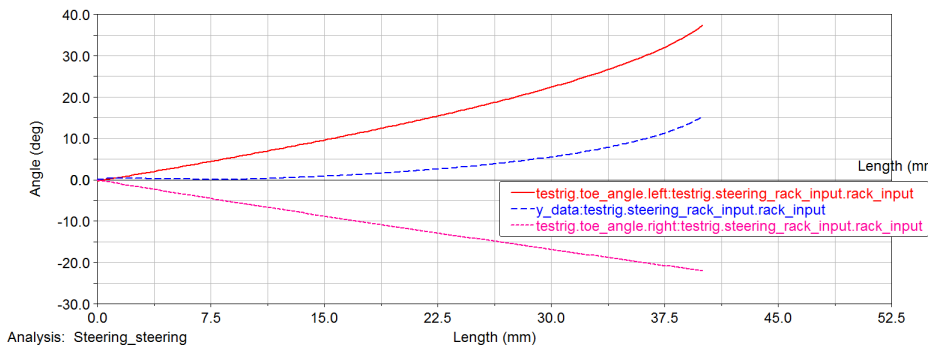
In Figure 5-2, a stability analysis has been done for each of the above scenarios. The cornering stiffness ratio has been chosen specifically to replicate all of the above situations.

Figure 5-2 shows how the eigenvalues move in the imaginary plane, depending on the velocity. For increasing velocity, it can be seen that for neutral-steer and under-steer, the eigenvalues of the lateral state matrix stay within the left half plane meaning it is a stable system. For an over-steered vehicle, the eigenvalues move into the right half plane for increasing velocity resulting into an unstable system.

The knowledge of the stability of the system is very essential for the design choice regarding tire selection. The chosen approach is to design the vehicle as an under-steered vehicle while using torque vectoring to decrease the induced yaw rate error. Therefore, tires with a higher cornering stiffness have been selected for the Forze VI. This decision results in the following equation:

$$\frac{m_f}{C_f} > \frac{m_r}{C_r} \rightarrow K_u > 0 \rightarrow \alpha_f > \alpha_r$$

This results into an under-steering vehicle. In the following section, a discussion will be held how to reduce the induced yaw rate error.

**Figure 5-3:** Forze VI Steering

5-1-3 Steering

In this subsection a model will be given which will be able to estimate the wheel angle δ . This will be done with the use of the knowledge of the sensor data from the steering wheel and with the information of the mechanical steering construction.

The steering wheel angle sensor is placed close to the rack and pinion. It is placed after one universal joint. The kinematics of the universal joint will be neglected. The angle that will be determined is the left and right angle of the wheels with the longitudinal axis of the vehicle.

The relation of this angle with the steering wheel angle depends on the rack-and-pinion ratio. The following relation exists between the rack displacement and the steering wheel rotation:

$$134\text{mm rack displacement} \triangleq 864^\circ \text{ pinion rotation} \quad (5-3)$$

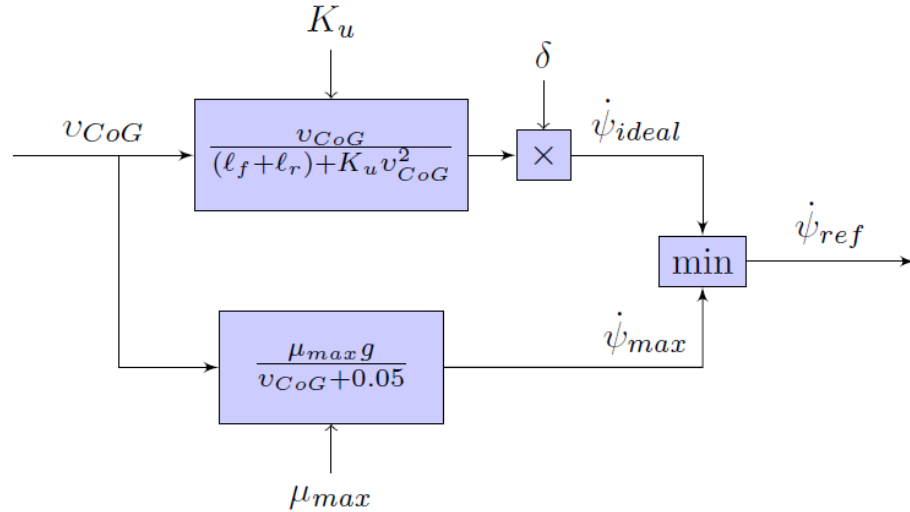
For an accurate fitting of both these curves a 9th order polynomial is used. This curve maps the relation between the rack displacement and the angle of the steer arm for the left and right wheel. In Figure 5-3 is shown that the displacement of the inner wheel is different from the outer wheel. In the case of a left turn the outer (right) wheel will have a larger displacement than the inner(left) wheel. This means that the Forze VI uses negative Ackermann steering.

The relation shown in Figure 5-3 only gives the angle of the steer arm of the inner and outer wheel and not the actual angle of the wheel. This relation will therefore not be sufficient to determine the wheel angle δ . To determine the wheel angle δ , the toe needs to be considered as well. The toe consist of a static part and a dynamic part. The static toe of the vehicle is implemented in the CarSim model. The values of the static toe is presented in Table 5-1.

The dynamic toe is depending on the suspension jounce and the steering arm angle. For the front wheel the effect of the steering arm angle is much more significant than the effect of the suspension jounce. The dynamic toe is approximated by a linear relation between the steering arm angle and the toe. This is done by measuring the wheel

Table 5-1: Static toe

Wheel	Toe angle [deg]
Front left	0.593
Front right	0.593

**Figure 5-4:** Pre-processor setup

angle δ of the vehicle for different steering wheel angles. The measured wheel angle is compared with the angle of the steering arm. The difference between these two angles are assumed to be the dynamic toe. The relationship between the dynamic toe and steering wheel angle seems relatively linear. Therefore, there is chosen to map this relationship with a linear function.

The pre-processor uses only the general steering angle of the front wheels, therefore an average of the two front steering angles will be taken. This will be done in the following way:

$$\delta = \frac{\delta_{fl} + \delta_{fr}}{2} \quad (5-4)$$

5-1-4 Desired vehicle behavior

Before a control algorithm will be determined, a reference signal needs to be defined in order to determine the controller performance. In the previous section it was determined how the steady-state stability of the vehicle was determined by the under-steer gradient. For steady-state stability of a vehicle, the under-steer gradient was set to be larger than 0. For optimal performance while maintaining stability, a neutral steering vehicle has the smallest possible turning radius at a certain velocity. Therefore, a neutral steered vehicle will be set as reference. The goal is to determine a method to describe the desired yaw rate with a function of known and measurable variables. The circular road

of radius can, with the under-steer gradient K_u , be used to determine the steady state steering angle. The under-steer gradient K_u is dependent on the cornering stiffness for each front and rear wheel.

$$\dot{\psi}_{des} = \frac{v_{CoG}}{R} \quad (5-5)$$

$$\frac{1}{R} = \frac{\delta}{(\ell_f + \ell_r) + K_u v_{CoG}^2} \quad (5-6)$$

$$K_u = \frac{\ell_r m}{C_f(\ell_f + \ell_r)} - \frac{\ell_f m}{C_r(\ell_f + \ell_r)} \quad (5-7)$$

Combining the expressions of the under-steer gradient and the circular road radius gives the following expression of $\dot{\psi}_{des}$. This expression of $\dot{\psi}_{des}$ is now dependent on the velocity v_{CoG} , under-steer gradient K_u and the steering angle δ .

$$\dot{\psi}_{des} = \frac{v_{CoG}}{(\ell_f + \ell_r) + K_u v_{CoG}^2} \delta \quad (5-8)$$

The desired yaw rate described in equation 5-8 cannot always be reached. In some cases it is not safe for the driver to try to obtain the desired yaw rate. For example, when the system tries to obtain the desired yaw rate when the tire-road friction coefficient is unable to provide the tire forces. A solution to this problem is to bound the yaw rate by its limiting factor. In the book of Rajamani [2] this limiting factor is the tire-road friction coefficient. In other words, the lateral movement, lateral acceleration, is bounded by the tire-road coefficient μ .

$$a_y = v_{CoG} \dot{\psi} + a_x \tan \beta + \frac{v_{CoG} \dot{\beta}}{\sqrt{1 + \tan^2 \beta}} \leq \mu \cdot g \quad (5-9)$$

In the equation of a_y the first part is dominating, this means that $v_{CoG} \dot{\psi}$ is a good approximation when the sideslip angles are small, hence the second and third term contribution to the lateral acceleration is very small. By rewriting these two equations, the following upper bound for the yaw rate can be constructed

$$\dot{\psi}_{max} = \sigma \frac{\mu \cdot g}{v_{CoG}} \quad (5-10)$$

By choosing the contribution factor σ for example 0.8, the first term will contribute 80% and the other two term for 20% to the total lateral acceleration. With this upper-bound for the yaw rate and the desired yaw rate a reference yaw rate can be constructed. This reference yaw rate will be the desired yaw rate as long as it does not exceed the upper bound of the yaw rate.

$$\dot{\psi}_{ref} = \begin{cases} \dot{\psi}_{des} & |\dot{\psi}_{des}| \leq |\dot{\psi}_{max}| \\ \pm \dot{\psi}_{max} & \text{otherwise} \end{cases} \quad (5-11)$$

5-2 Yaw rate control

For the analysis of the vehicle dynamics and the design of observers or control-algorithms, the equations of motion are needed and the physical interactions between the various subsystems must be written in the form of mathematical equations. To make the analysis as clear as possible, simplifications are required. The choice of simplification defines the model. The fact that there is limited knowledge of the vehicle parameters and little knowledge of the tire parameters a linear bicycle model is chosen. A suitable linear vehicle model is the linear bicycle model.

The linear bicycle model is a single track vehicle model. In this model, the assumption is made that a vehicle consists of only a front and a rear-wheel. There is no distinction between the left and right wheels. In this form, the dynamics of the system are less complicated, this makes it easier to get stability insights and tuning linear control laws. This model is extracted from the literature [4, p. 150]. In table 5-2, the terminology used in the equations of motion is introduced.

Table 5-2: Terminology used in equations of motion

Term	Symbol	Units
Yaw rate	$\dot{\psi}$	[rad s ⁻¹]
Sideslip angle	β	[rad]
Velocity at Center of Gravity (CoG)	v_{CoG}	[m s ⁻¹]
Yaw moment	M_z	[N m]
Steering angle	δ	[rad]
Slip angle	α_i	[rad]
Longitudinal force	$F_{x,ij}$	[N]
Lateral force	$F_{y,ij}$	[N]
Vehicle mass	m	[N]
Inertia moment	J_z	[kg m ²]
Cornering stiffness	C_i	[N rad ⁻¹]

The lateral forces are proportional to the slip angle when the friction utilization is low, but will saturate at a constant level for large slip angles. When the vehicle velocity slowly changes, only the yaw rate and lateral dynamics will be important in the single-track model. This means that the longitudinal vehicle velocity v_{CoG} can be considered as a known parameter. For the linearized single-track model a linear tire model will be used:

$$F_{y,i} = C_i \alpha_i \quad (5-12)$$

The corresponding equations are denoted in equation 5-14. In the equation, the state vector is denoted as $x = [\beta \dot{\psi}]^T$ and the inputs as $u_1 = \delta$ and $u_2 = M_z$. The input u_1 is the default steering input. Input u_2 is the added momentum on the vehicle as a result of the inequality of the individual wheel forces. This is fundamental for the torque vectoring control of the Forze VI and will be used later on for control purposes.

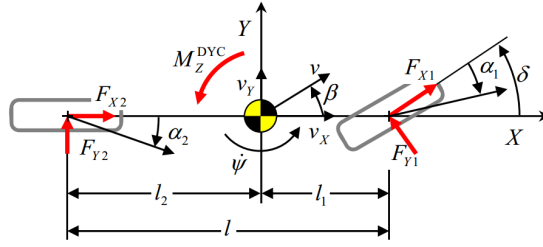


Figure 5-5: Single-track Vehicle model [5]

$$\begin{aligned} J_z \ddot{\psi} &= (\ell_f C_f - \ell_r C_r) \beta + \frac{1}{v_{CoG}} (\ell_f^2 C_f - \ell_r^2 C_r) \dot{\psi} - \ell_f C_f \delta \quad (5-13) \\ m v_{CoG} (\dot{\psi} + \dot{\beta}) &= (C_f + C_r) \beta + \frac{1}{v_{CoG}} (\ell_f C_f - \ell_r C_r \dot{\psi}) - C_f \delta \end{aligned}$$

With the equations of motion in 5-14, the following state-space model is constructed:

$$\dot{x} = Ax + Bu_1 + Eu_2 \quad (5-14)$$

where the state and input vector are:

$$x = \begin{bmatrix} \beta \\ \dot{\psi} \end{bmatrix} \quad u_1 = [\delta] \quad u_2 = [M_z]$$

and

$$A = \begin{bmatrix} \frac{-(C_r + C_f)}{mv_{CoG}} & \frac{-(C_r \ell_r + C_f \ell_f)}{v_{CoG}^2} - 1 \\ \frac{-(C_r \ell_r + C_f \ell_f)}{J_z} & \frac{-(C_r \ell_r^2 + C_f \ell_f^2)}{J_z v_{CoG}} \end{bmatrix} \quad B = \begin{bmatrix} \frac{C_f}{mv_{CoG}} \\ \frac{C_f \ell_f}{J_z} \end{bmatrix} \quad E = \begin{bmatrix} 0 \\ \frac{1}{J_z} \end{bmatrix}$$

For the yaw rate control there is chosen to take the steering input δ as a disturbance and not as a controlled input. The reason for this is that the driver cannot be controlled by the system, because it acts on his own. This means that there is no feedback possible for the steering input in the current setup. When the steering angle δ is modeled as disturbance the linear vehicle model described in 5-14, the following state space model is chosen:

$$\dot{x} = Ax + Eu_2 \quad (5-15)$$

For this linear bicycle model a linear control method will be used. There is chosen a Proportional Integral Derivative (PID) controller for this system. It is a simple and very versatile controller, that can easily be tuned during tests. Because the model has an internal derivative action, there is no need for a D action. The PID controller is simplified to only a Proportional Integral (PI) controller. The goal of the controller is to ensure good tracking of the yaw rate $\dot{\psi}$. The goal is to achieve an overshoot of less than 5% and a settling time of 0.2s. This corresponds to a bandwidth of 5 Hz. The

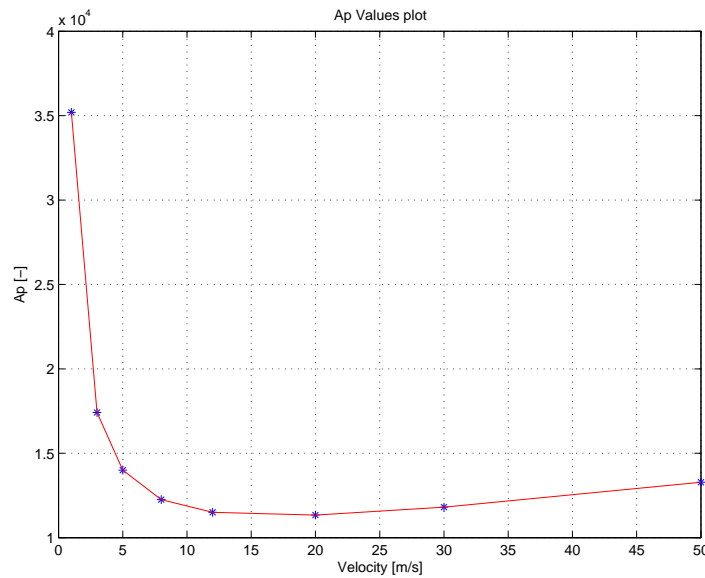


Figure 5-6: plot of the fit of the Ap values of the controller, with the mapping function

5 Hz bandwidth is chosen because the motor controller operates at 100 Hz. A hand-rule in control theory states that there should be atleast a factor of 10 between frequency of the controlled plant and the controller. The control bandwidth is chosen smaller then 10 Hz because the frequency of the tire dynamics is close to 10 Hz. Around 10 Hz the non linear tire dynamics becomes more present and can interfere or act on the control input.

Because the linear bicycle model is only valid for a certain velocity set-point, one controller will not be accurate enough to control the vehicle. Therefore a gain scheduled controller is constructed. There is chosen for 8 difference velocity set-points within the velocity range of the vehicle of 0 to 220 km/h.

$$v_{ctrl} = [1 \ 3 \ 5 \ 8 \ 12 \ 20 \ 30 \ 60] [\text{m s}^{-1}]$$

There are more set-points in the lower region because in that region the model is more sensitive of the velocity. To get better performance more set-points are needed in the low velocity region. The values of the P and I are determined with a bode plot analysis. The P and I values are chosen such that the open-loop system has a bandwidth of 5 Hz and a phase margin of 60° . After tuning 8 PI controllers the P and I values are placed in a graph with the set-point speed of each corresponding controller on the x-axis, see Figure 5-6 and Figure 5-7. With these graphs two continuous function are made that map the P an I values for each set-point speed. In this case for each velocity the two continuous functions give the right P and I values to construct the desired PI controller.

With this two constructed continuos functions, the step response of the closed loop system is tested by performing a step for eight random velocities. In Figure 5-8 these eight step responses show almost identical responses, which concludes that the mapping function are chosen correctly.

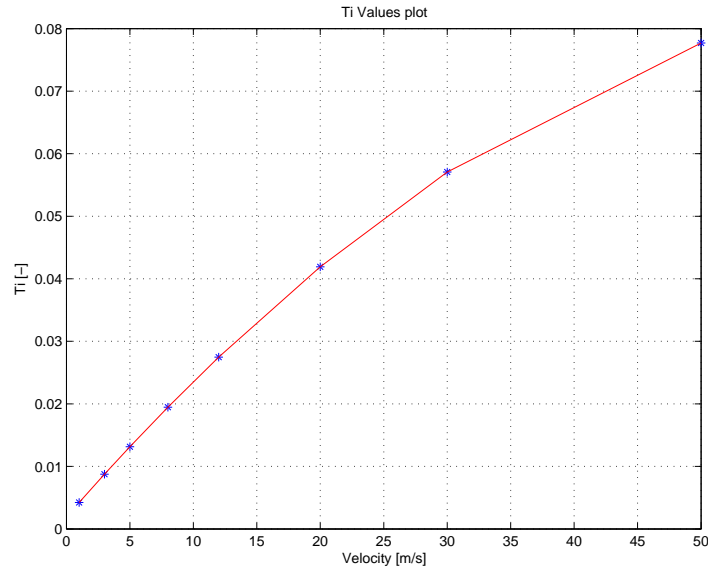


Figure 5-7: plot of the fit of the T_i values of the controller, with the mapping function

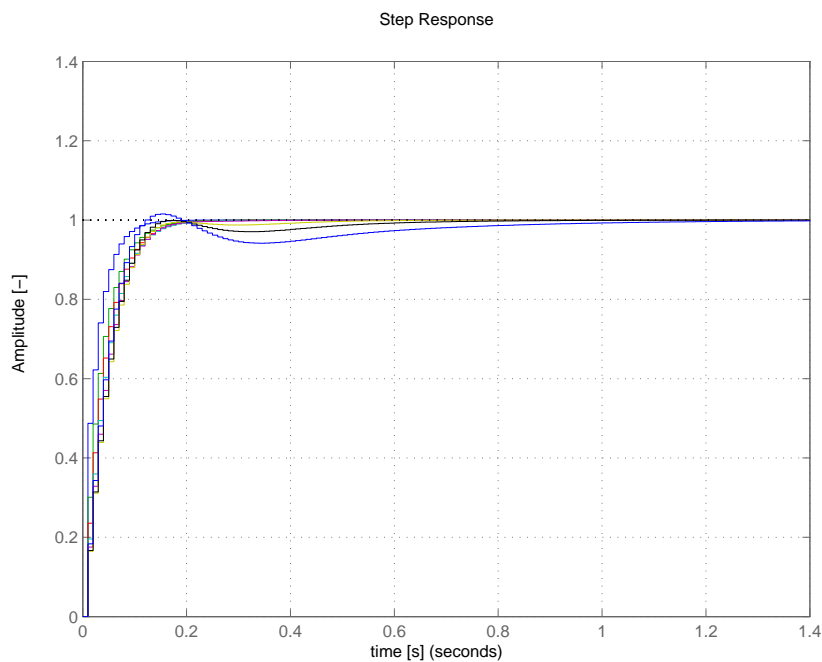
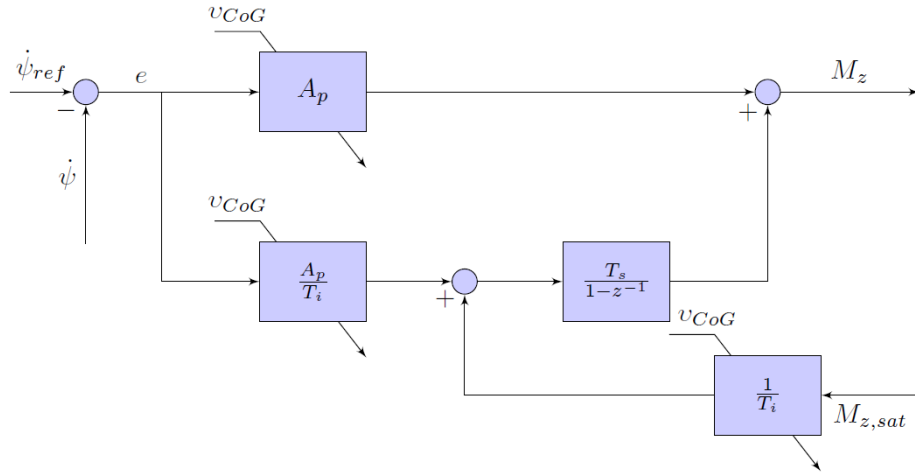


Figure 5-8: plot of the step response of the closed loop system

**Figure 5-9:** PID controller

Because the control output, M_z can not always be reached due to limiting factors of the electrical motors and/or the tires, the integrating action of the controller is building up. This is unwanted behavior. When the integrating action is building up and the error drops the control output will still be high. To prevent this an anti-windup algorithm is build in the controller. This anti-windup will subtract the difference between the value of M_z at the controller output and the achieved M_z , this error is called $M_{z,sat}$. In this way the integrating action will not build up because the input of the integrator is now adjusted/corrected to the limiting factors of the motors and/or the tires. The integrator input then becomes:

$$\frac{1}{T_t} M_{z,sat} + \frac{A_p}{T_i} e \quad (5-16)$$

$$M_{z,sat} = \frac{-A_p T_t}{T_i} e \quad (5-17)$$

With $M_{z,pp}$ the actual yaw moment output of the post-processor and knowing that $M_{z,sat} = M_{z,pp} - M_z$, the new control output becomes:

$$M_z = M_{z,pp} + \frac{A_p T_t}{T_i} e \quad (5-18)$$

Remark, the steering input has been chosen to be a disturbance. Therefore, the controller does not take into account the influence of the steering angle δ on the system. The influence of the steering angle on the system can be seen as a feed-forward term. This means that the controller will behave more aggressively on the real model than on the model used for the control. To reduce this effect, the P action must be reduced.

5-3 Post-processor

In the post-processor, the M_z that the yaw rate controller produces will be translated to the wheel torques of the vehicle. This is not a straightforward process, because the

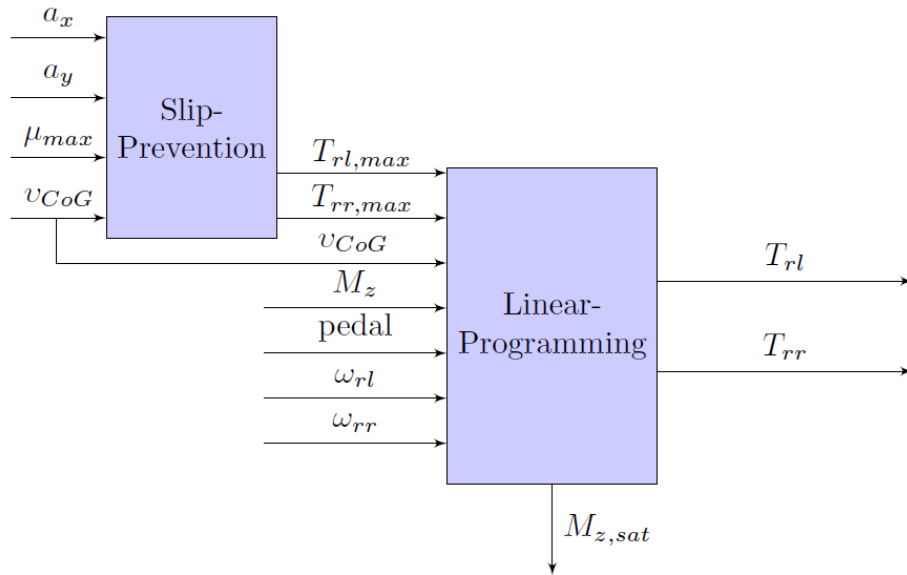


Figure 5-10: Post-processor setup

M_z from the controller does not take the power limitations into account of the motors and the tire limitations. Therefore the post processor consist of two different parts. The first part determines the amount of torque that can be applied without the tires slipping. This is done by determining the weight shifts of the vehicle, by a geometric approach. The other part consist of a linear programming algorithm which handles the constraint from the slip control, power limitations, and the limitation from the buffer and fuel cell system.

The post-processor handles the output of the controller, hence the mapping of $M_z \rightarrow \{T_{rl}, T_{rr}\}$. All actuator limits and slip-ratio control are handled in this subroutine.

5-3-1 Slip prevention

In order to prevent the wheels from slipping, the dynamic wheel loads must be calculated. The wheel loads are very important in determining the maximum steady-state cornering capabilities. These wheel loads can be translated to wheel torques. These wheel torques then represents the maximum torques for steady-state cornering, without slipping. The wheel loads are constantly changing, and in order to model these changes, assumptions are made. This means steady-state operating conditions, with a vehicle in steady-state with a rigid chassis. Other assumptions are that all the basic vehicle data such as roll rates, spring rates, etc. are linear and that the dimensional data of the vehicle is constant. The last, and one of the most important assumptions is that the principle of superposition is valid. This principle states that the total of a series of effects considering concurrently is identical to the sum of the individual effects considering individuality. Which means that the changes in lateral, longitudinal, aerodynamic load transfers, are valid to combine to one load transfer.

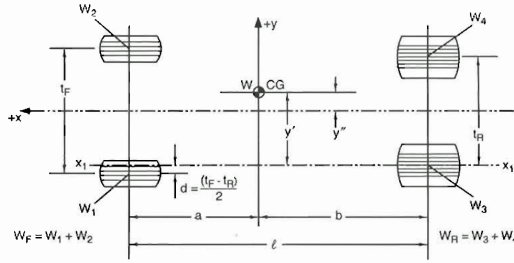


Figure 5-11: schematic overview of the vehicle, with wheel loads

Static load

The first wheel loads that can be determined are the static wheel loads. The total vehicle weight is the sum of the four individual wheels weights.

$$W_{fl} + W_{fr} + W_{rl} + W_{rr} = W \quad (5-19)$$

where $W_F = W_{fl} + W_{fr}$ and $W_R = W_{rl} + W_{rr}$

Looking at the moment around the rear axle, there can be seen that this relation holds:

$$\ell_f = \frac{W_F \ell}{W} \text{ where } \ell_r = \ell - \ell_f \quad (5-20)$$

With these two equations all the static wheel loads can be determined as follows:

$$\begin{aligned} W_{s,fl} &= \frac{\ell_f}{2\ell} W \\ W_{s,fr} &= W_{s,fl} \\ W_{s,rl} &= \frac{\ell_r}{2\ell} W \\ W_{s,rr} &= W_{s,rl} \end{aligned} \quad (5-21)$$

For further calculations of the dynamic wheel loads, the position of the CoG and the sprung mass center of gravity are needed. The CoG is known for this vehicle and is $h = 0.335$, the sprung mass CoG needs to be calculated. For the calculation of the sprung mass CoG the weight of the unsprung masses(wheels, tires, brakes) are needed. These are unfortunately unknown. An alternative to calculate the sprung mass CoG is to use the roll centers height and the geometric property's of the vehicle.

$$h = 0.335 \quad (5-22)$$

$$H = h - \frac{\ell_r}{\ell z_{rr}} - \frac{\ell_f}{\ell z_{rf}}$$

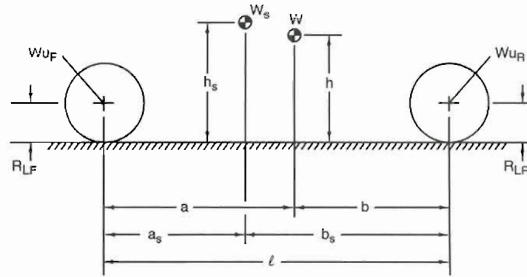


Figure 5-12: sprung mass center of height

Lateral load transfer If a vehicle takes a turn, the load is transferred from the inside pair of wheels to the outside pair of wheels, when the car's CoG is above the ground. This is due to the centrifugal force, which is an result of opposing the lateral acceleration produced by the tire cornering force. In Figure 5-13 there is schematic view of rear axle. The cornering force produce by the tires $S_l + S_r$ results in a lateral acceleration A_Y (in "g"), this results in lateral wheel load transfer of:

$$\begin{aligned} W_y &= \frac{W}{2} + \frac{WA_Yh}{t} \\ \Delta W &= W_L - \frac{W}{2} = \frac{WA_Yh}{t} \end{aligned} \quad (5-23)$$

where ΔW is the increase in left side load and decrease in right side load due to cornering.

The load transfer described in (5-24) is only valid for steady-state turns, because this equations does not consider for combined lateral and longitudinal accelerations or other dynamic effects. Two different mechanisms can be used to calculate the effect on the wheel loads. The first mechanism is through the springs in proportion to relative front and rear roll stiffness. The second mechanism utilizes the direct application of loads, from the tires, to the chassis through the suspension members as determined by the heights of the front and rear roll centers. So to describe the loads for all four wheels the roll center height and roll stiffness are required, which are known for our vehicle.

The vehicle will be treated as a single mass system, because there is not enough detailed information about the geometry of the vehicle. So in our model we assume that the total vehicle CoG is above the neutral roll axis. So for the lateral wheel load transfers we have the following equations:

$$\begin{aligned} W_{y,fl} &= \frac{W}{t_f} \left[\frac{HK_{rf}}{K_{rf} + K_{rr}} + \frac{\ell_f}{\ell} z_{rf} \right] A_Y \\ W_{y,fr} &= -W_{y,fl} \\ W_{y,rl} &= \frac{W}{t_r} \left[\frac{HK_{rr}}{K_{rf} + K_{rr}} + \frac{\ell_r}{\ell} z_{rr} \right] A_Y \\ W_{y,rr} &= -W_{y,rl} \end{aligned} \quad (5-24)$$

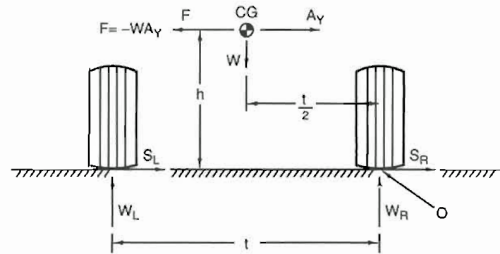


Figure 5-13: total lateral load transfer

Longitudinal load transfer When the vehicle is pulling up, there is a positive acceleration. Adversely there is a negative acceleration. Under acceleration an internal reaction force is created, similar to the centrifugal force under cornering. So under longitudinal acceleration the wheel load transfer are:

$$\begin{aligned} W_{x,fl} &= -\frac{h}{2\ell} Wa_x \\ W_{x,fr} &= W_{x,fl} \\ W_{x,rl} &= \frac{h}{2\ell} Wa_x \\ W_{x,rr} &= W_{x,rl} \end{aligned} \quad (5-25)$$

Aerodynamic loads By the Society of Automotive Engineers (SAE) the aerodynamic axis is located in the ground plane at the center of the four wheels. With this axis only the pitch, roll moments and overall lift effect wheel loads.

Table 5-3: Terminology aerodynamic parameters

Symbol	description
q	dynamic pressure
A	reference frontal area
ℓ	wheelbase
$C_{l,i}$	lift coefficient
C_{rm}	roll moment coefficient

In racing applications overall lift and pitching moments are usually combined into separate front and rear lift. These act at the respective axle locations and are calculated from:

$$\begin{aligned} LF &= C_{l,f} q A \\ LR &= C_{l,r} q A \\ Rm &= C_{rm} q A \ell \end{aligned} \quad (5-26)$$

A positive aerodynamic rolling moment increases loads on the right side and decreases loads on the left side. These rolling moments are distributed to the front and rear axle in proportion to the roll stiffness:

$$\begin{aligned} W_{aero,fl} &= -\frac{LF}{2} + \frac{K_{rf}}{K_{rf} + K_{rr}} \left(\frac{Rm}{t_f} \right) \\ W_{aero,fr} &= -\frac{LF}{2} - \frac{K_{rf}}{K_{rf} + K_{rr}} \left(\frac{Rm}{t_f} \right) \\ W_{aero,rl} &= -\frac{LR}{2} + \frac{K_{rr}}{K_{rf} + K_{rr}} \left(\frac{Rm}{t_r} \right) \\ W_{aero,rr} &= -\frac{LR}{2} - \frac{K_{rr}}{K_{rf} + K_{rr}} \left(\frac{Rm}{t_r} \right) \end{aligned} \quad (5-27)$$

Anti-roll bar load transfer The weight shift describer above are all depending on the distribution of ride and roll rates. All these calculation ride rates are not taken into account. These ride rates determine the wheel load experienced by the vehicle and the wheel travel allowed in racing situations. The roll bar is designed to ensure safety for the driver but also to ensure the desired roll rates. By installing an anti-roll bar the suspension rates change, which therefore change the roll rates of the vehicle. With these new roll rates the effect of the anti-roll bar on the wheel loads can be determined by the deference between the old roll rate and the new roll rates with anti-roll bar:

Table 5-4: Terminology anti-roll bar parameters

Symbol	Description	Units
K_{wf}	front wheel rate	[N m ⁻¹]
K_{wr}	rear wheel rate	[N m ⁻¹]
$K_{rf,A}$	front ARB stiffness	[N m rad ⁻¹]
$K_{rr,A}$	rear ARB stiffness	[N m rad ⁻¹]

$$\begin{aligned} W_{ab,fl} &= K_{rf,A}/(K_{rf,A} + \frac{K_{wf}t_f^2}{2})W_{y,fl}; \\ W_{ab,fr} &= -W_{ab,fl}; \\ W_{ab,rl} &= K_{rr,A}/(K_{rr,A} + \frac{K_{wr}t_r^2}{2})W_{y,rl}; \\ W_{ab,rr} &= -W_{ab,rl}; \end{aligned} \quad (5-28)$$

With all the wheel load transfers calculated, the super position definition can be used to determine the total individual wheel loads of the vehicle:

$$\begin{aligned} W_{fl} &= W_{s,fl} + W_{y,fl} + W_{ab,fl} + W_{x,fl} + W_{aero,fl} \\ W_{fr} &= W_{s,fr} + W_{y,fr} + W_{ab,fr} + W_{x,fr} + W_{aero,fr} \\ W_{rl} &= W_{s,rl} + W_{y,rl} + W_{ab,rl} + W_{x,rl} + W_{aero,rl} \\ W_{rr} &= W_{s,rr} + W_{y,rr} + W_{ab,rr} + W_{x,rr} + W_{aero,rr} \end{aligned} \quad (5-29)$$

These wheel loads can now be translated to the longitudinal wheel forces. This is done with the following relation:

$$F_{x,ij} = W_{ij}\mu \quad (5-30)$$

The longitudinal force $F_{x,ij}$ represent the tracking of each wheel. With the relation for $F_{x,ij}$ in (5-31) the traction circle of the wheel will be squared. That means that for lateral wheel loads, the longitudinal force $F_{x,ij}$ stays constant. In reality the longitudinal force $F_{x,ij}$, reduces by higher lateral wheel loads. Because no lateral wheel forces are known the correction is done the following way:

$$\begin{aligned} F_{x,rl} &= \sqrt{W_{rl}^2\mu^2 - W_{rl}^2A_Y^2} \\ F_{x,rr} &= \sqrt{W_{rr}^2\mu^2 - W_{rr}^2A_Y^2} \end{aligned} \quad (5-31)$$

With the adjusted longitudinal forces $F_{x,lr}$ and $F_{x,rr}$ the wheel torques can be calculated. These wheel torque are the maximum allowed torques on the wheel without the wheel losing traction. These maximum wheel torques are the dynamic constraints for the Linear Programming (LP) discussed in the next section. Because the Force VI is a Rear Wheel Drive (RWD) racing vehicle only, there are no torque constraints for the front wheels. For the calculation of the wheel torques, a constant effective tire radius is assumed.

$$\begin{aligned} T_{max,rl} &= F_{x,rl} \cdot r_{eff,r} \\ T_{max,rr} &= F_{x,rr} \cdot r_{eff,r} \end{aligned} \quad (5-32)$$

5-3-2 Electrical motor model

Besides the constraint of the slip control, the motor is a limiting factor as well. The motor can not exceed the maximum rotational velocity or maximum power. Other limitations of the motors are the amount of torque they are capable of delivering. Not all the constraints are from the motor, the fuel cell and the buffer also create constraints. These constraints are related to the maximum amount of power that can be supplied to the motors. This results into the following constraints:

Table 5-5: Terminology used in equations of motion

Variable	Constraint
minimum speed left and right motor	0 rpm
maximum speed left and right motor	7500 rpm
maximum torque left and right motor	400 N m
maximum torque vehicle	800 N m
maximum power vehicle	190 kW

note: the maximum power of the vehicle is depending on the buffer level, so in theory the maximum power of the vehicle is as follows:

$$\text{maximum power vehicle} = 190 \text{ Kw} - (1 - \text{buffer level}) \cdot \text{buffer capacity}$$

The torques for both wheels are further limited by speed, current and power. The torque is limited by a linear ramp near the speed limits. The inputs for these maximum torque curves are the maximum power as computed in power scaling over DC voltage, see Figure 5-14. The torque limit has the general expression of:

$$T_{max}(\omega) = \min(T_{max}, \frac{P_{max}}{|\omega|}) \quad (5-33)$$

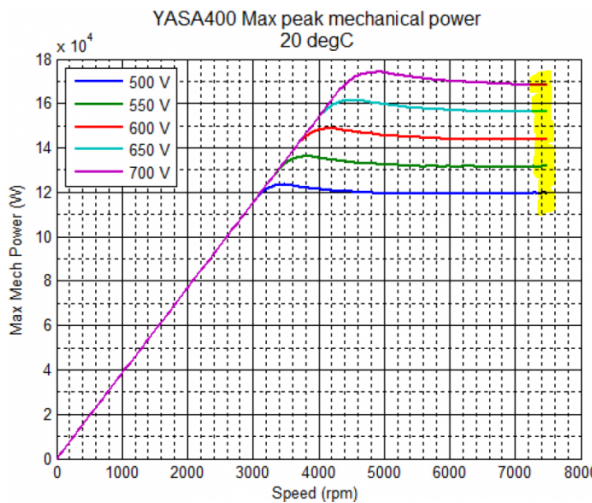


Figure 5-14: The maximum power curves depends on the speed and the input voltage. The yellow marking is the power used in the torque vectoring algorithms

The half-shaft dynamics are not taking into account. This means that the torque from the controller is put directly on the wheels. The assumption is made that an Active Vibration Control (AVC) is used to cope with the half-shaft dynamics [6].

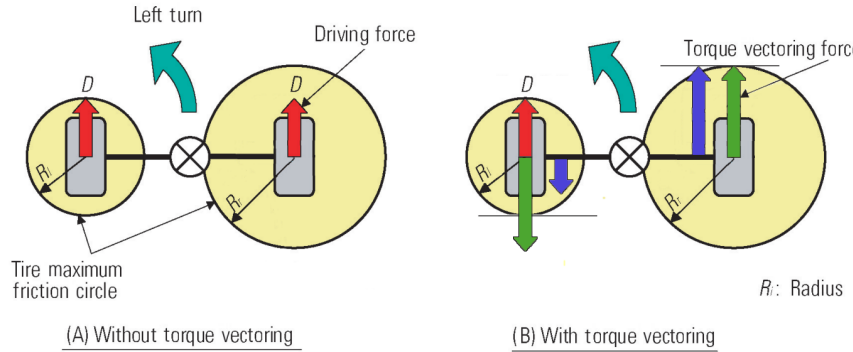


Figure 5-15: Torque vectoring where M_z guaranteed

5-3-3 Linear programming control

With all the constraints known the linear programming problem can be constructed. The torque distribution can be written as a linear optimization problem with equality and inequality constraints. The constraint used in this LP problem are all torque position related. There are no constraints considered for the the torque rate. Distinction can be made with two different goals. The first goal is optimizing for the net moment around the CoG of the vehicle. The second goal is optimizing the driving torque that is applied to the road. Therefore two optimization problems are used for the mapping. To start, the demanded yaw moment M_z of the controller around the CoG is transformed to net torque vectoring torque $TV_{control}$ to be applied on the wheels.

$$TV_{control} = \frac{M_z r_{eff,r}}{2s_r G_r} \quad (5-34)$$

With G_r the gear ratio, $r_{eff,r}$ the effective wheel radius of the rear tires, s_r the lateral distance between the wheel and the CoG and M_z the yaw moment from the controller.

1. Guarantee M_z demand The first linear programming routine ensures the desired yaw moment M_z or the maximum yaw moment allowed by all the constraints. Besides the guarantee of the maximum yaw moment M_z , the routine maximizes also tries to maximize the amount of drive torque. To ensure maximum torque vectoring torque the maximum allowed torque is calculated as follows:

$$TV_{max} = \min(400, (T_{max,rr} + T_{max,rl})/2); \quad (5-35)$$

Because TV_{max} does not consider the demanded drive torque T_{tot} , it is possible that for a low drive torque demand, the LP is not able to find a solution. The optimal drive torque would then be larger the the demanded drive torque T_{tot} . To ensure the total drive torque not to become larger then the demanded drive torque T_{tot} , an exact penalty

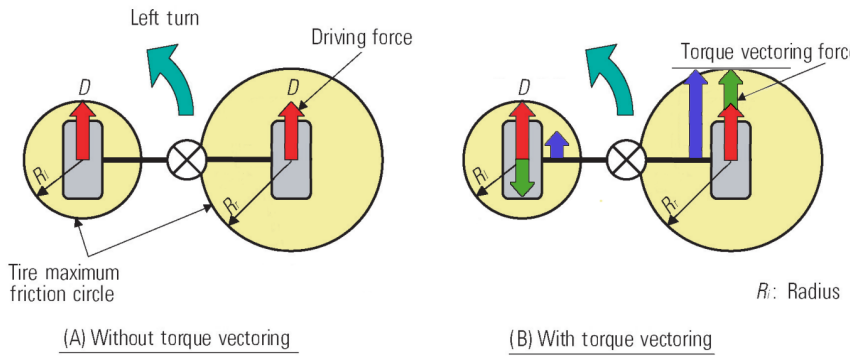


Figure 5-16: Torque vectoring where T_{tot} guaranteed

function will be introduced to reduce the torque vectoring torque, when necessary.

$$\begin{aligned} & \max_{T_{rl,1}, T_{rr,1}} \quad T_{rr,1} + T_{rl,1} + \epsilon \\ \text{subject to} \quad & -T_{max,rr} \leq T_{rr,1} \leq T_{max,rr} \\ & -T_{max,rl} \leq T_{rl,1} \leq T_{max,rl} \\ & T_{rr,1} + T_{rl,1} \leq T_{max} \\ & T_{rr,1} - T_{rl,1} + \epsilon = 2 \cdot \max(-TV_{max}, \min(TV_{max}, TV_{control})) \\ & \epsilon \geq 0 \end{aligned}$$

2. Guarantee torque demand The second linear programming routine, ensures the maximum drive torque to the road, by the demand of the driver. This is done by setting the maximum torque vectoring torque as follows:

$$TV_{max} = \max(0, \min(400, (T_{max,rl} - T_{tot}/2), (T_{max,rr} + T_{tot}/2))); \quad (5-36)$$

By subtracting the demanded drive torque T_{tot} of the diver from the friction circle, the drive torque will always be exactly the demanded drive torque. In this case it is more likely that the desired yaw moment M_z will be reached. It is even possible if the drive torque demand is too high, no torque vectoring torque will be applied.

$$\begin{aligned} & \max_{T_{rl,2}, T_{rr,2}} \quad T_{rr,2} + T_{rl,2} \\ \text{subject to} \quad & -T_{max,rr} \leq T_{rr,2} \leq T_{max,rr} \\ & -T_{max,rl} \leq T_{rl,2} \leq T_{max,rl} \\ & T_{rr,2} + T_{rl,2} \leq T_{max} \\ & T_{rr,2} - T_{rl,2} = 2 \cdot \max(-TV_{max}, \min(TV_{max}, TV_{control})) \end{aligned}$$

These two linear optimization problems both calculate two different torques, the first optimized for maximum M_z and the second optimized for the demanded drive torques T_{tot} . The controller which optimizes the yaw moment M_z , does not have the total drive torque constraint, which means that the driver is not in control over the drive torque.

This can feel unnaturally and could be a problem for the driver. Therefore a κ values is introduced so that the driver can adjust the influence of both linear optimization problems. This will be done in the following way:

$$\begin{aligned} T_{rl} &= T_{rl,1}\kappa + T_{rl,2}(1 - \kappa) \\ T_{rr} &= T_{rr,1}\kappa + T_{rr,2}(1 - \kappa) \end{aligned} \quad (5-37)$$

Note: In LabVIEW the "linear programming" function has an extra constraint conflicting with the linear optimization problems above. This constraint concerns the solution vector $x \geq 0$. This is circumvented by the introduction of slack variables. T_{rl} is written as $T_{sv,pos} - T_{rl,neg}$, with $T_{sv,pos} = 400 \text{ N m}$, the same is done for T_{rr} . The value of the slack variable is the maximum allowable torque at all time, such that the solution vector is always positive. This makes the actual algorithm somewhat more extensive but not any different in the results.

Chapter 6

Results PI and LP Controller

In this Chapter, the simulation results of the PI and Linear Programming (LP) controller will be presented. In this Chapter 4 different simulations will be presented. All these simulation are done with the use of CarSim and LabVIEW. The commands come from CarSim and are simulated in a non real-time simulation in LabVIEW. Different pre-programmed maneuvers will be used in CarSim to show the vehicle behavior for the three different cases: no torque vectoring, torque vectoring with $\kappa = 0$ and torque vectoring with $\kappa = 1$.

6-1 Step response

The first simulation is a step response test. In the first test the vehicle will begin with an initial velocity of 60 km h^{-1} which will be maintained the entire run. During the run a step on the steering wheel is set. The first step response test is executed for a steer input step of 10° . In the second test the vehicle will begin with an initial velocity of 80 km h^{-1} which will be maintained the entire run. During the run a step on the steering wheel is set. The first step response test is executed for a steer input step of 30° . In both runs the buffer capacity is included in the total power of the vehicle, so the vehicle runs on full power.

In Figure 6-1 and Figure 6-2 the simulation results of a 10 degrees steering step input are shown. In the first subplot the reference tracking is shown. When after 3 sec the steering input of 10 degrees occurs, the vehicle without torque vectoring is not capable of reaching the reference yaw rate. The vehicle with torque vectoring $\kappa = 0$, indicated as TV(0), is capable of reaching the reference yaw rate. This is done in 0.41 seconds and with a overshoot of 9.2%. The same holds for torque vectoring with $\kappa = 1$, indicated with TV(1). This is due to the fact that the drive torque for a constant speed of 60 km h^{-1} is low. Because the drive torque is low, TV(0) and TV(1) are identical. When these values are compared to the linear step response values there are not a

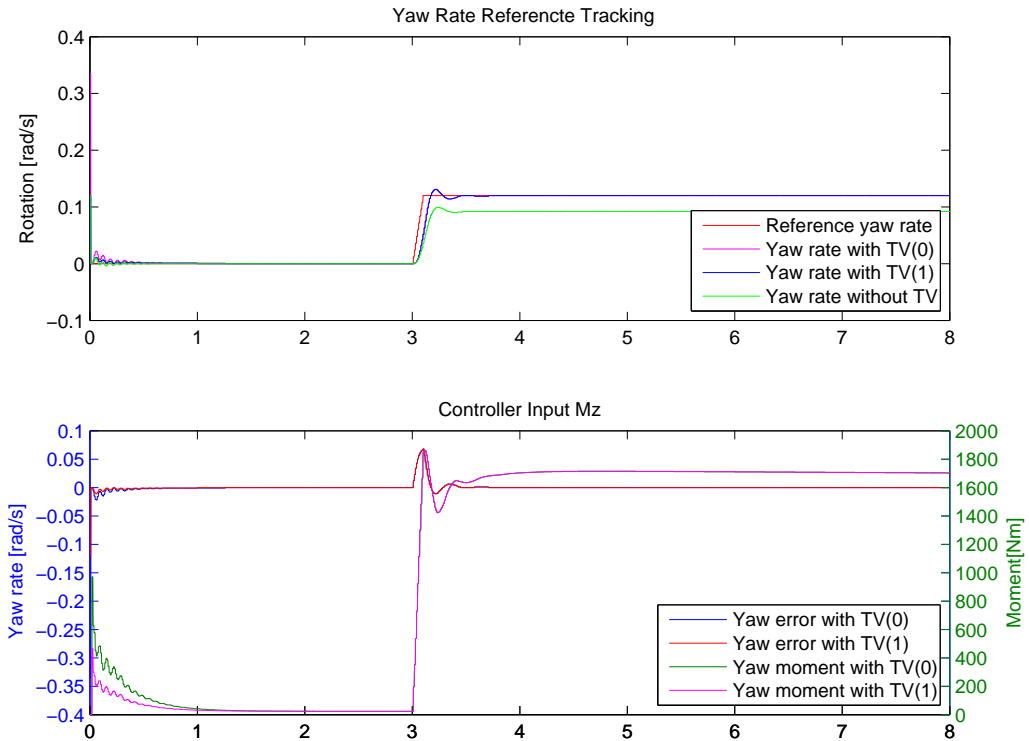


Figure 6-1: Plot of the yaw rate tracking and controller in/output for a step response of 10°

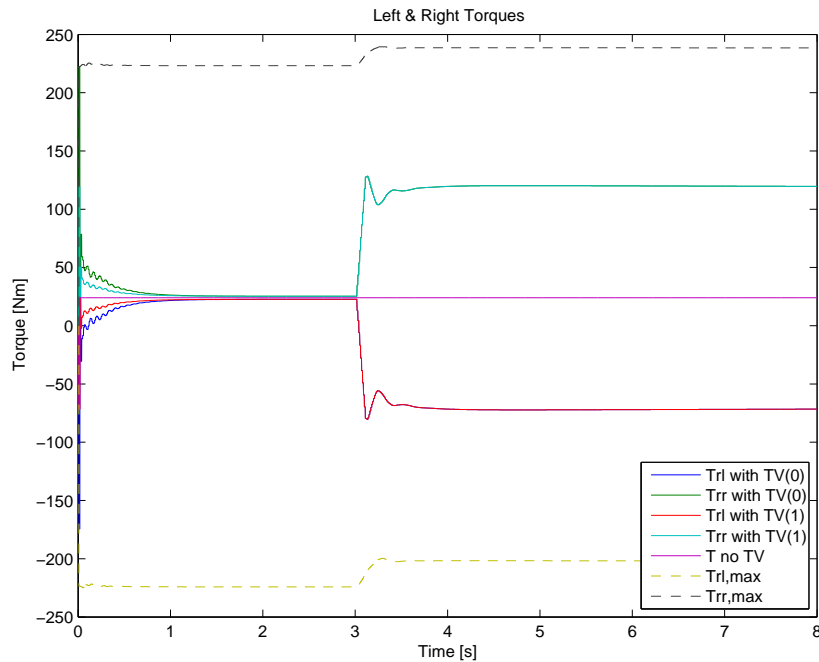


Figure 6-2: Plot of the torques for a step response of 10°

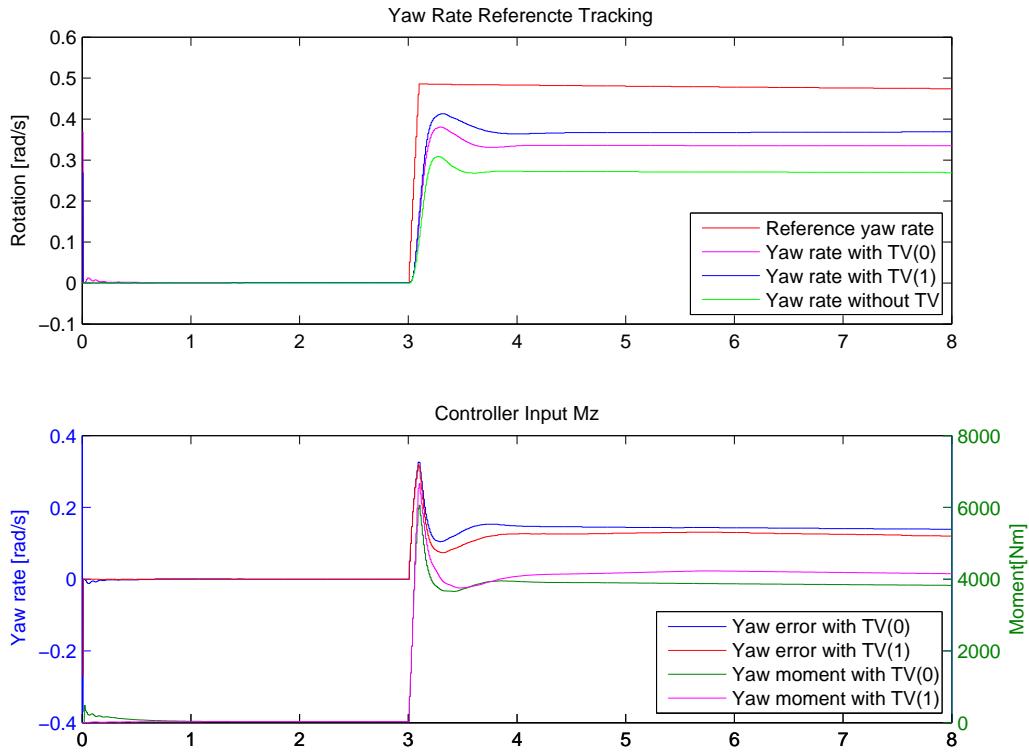


Figure 6-3: Plot of the yaw rate tracking and controller in/output for a step response of 30°

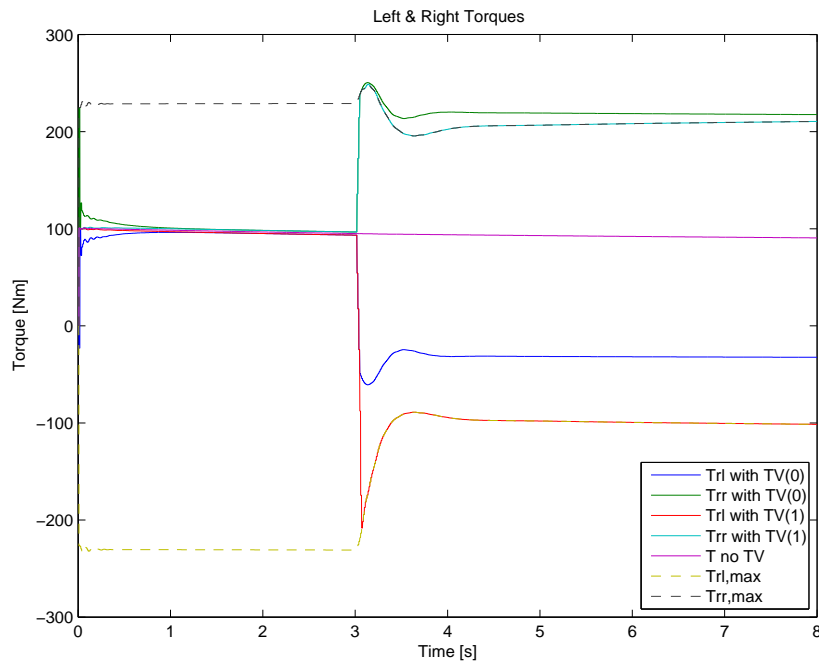


Figure 6-4: Plot of the torques for a step response of 30°

match. The values of the non-linear simulation are higher. An explanation can be found in the role of the steer angle δ and the non-linear effect of the real vehicle model.

In the other subplot the controller input(yaw rate error) and output(yaw moment) are presented. For this simulation both yaw rate errors of TV(0) and TV(1) converges to zero. This subplots confirms that TV(0) and TV(1) are identical. Figure 6-2 shows that the demanded torque by the controller is within in the bounds of the maximum allowed torque from the slip controller.

In Figure 6-1 and Figure 6-2 the simulation results of a 30 degrees steering step input are shown. In the first subplot we see the same characteristic of the vehicle without torque vectoring as for the lower speed and small steering input of 10 degrees. For the the vehicle with torque vectoring TV(0) and TV(1) the yaw rate error no longer converges to zero. The reference signal can no longer be tracked perfectly which was the case for the low speed and small steering angle of 10 degrees. This is due to the fact that the demanded torques of the controller can no longer be reached. These torques are now restricted by the maximum allowed torques from the slip controller. The actual yaw moment M_z is now smaller then desired yaw moment from the output of the controller. Furthermore TV(0) and TV(1) are no longer identical, that is because the drive torque has been increased. TV(0) always insures the demanded drive torque where TV(1) provides the largest torque vectoring torque.

6-2 Constant steer input

In this simulation a constant steering wheel input is set on the vehicle to simulate corner behavior. In this test the vehicle will begin with an initial velocity of 90 km h^{-1} which will be maintained the entire run. During the entire run the angle on the steering wheel is constant. The cornering test is executed 2 times for a constant steer input of 10° and 30° . In all the runs the buffer capacity is included in the total power of the vehicle, so the vehicle runs on full power.

In Figure 6-5 the simulation results of a constant steering input of 10 degrees is shown. In the case of no torque vectoring the reference yaw rate can not be reached. This results in a smaller corner radius then the vehicle with torque vectoring; TV(0) and TV(1). Neither of the vehicles with torque vectoring are capable of tracking the reference yaw rate, but for TV(1) it is very close. What this simulation shows is the increase in lateral acceleration, or g force, generated by the torque vectoring torque.

In Figure 6-6 the simulation results of a constant steering input of 30 degrees is shown. In the case of no torque vectoring the reference yaw rate can again not be reached, the same holds for TV(0) and TV(1). For the vehicle with torque vectoring this is also the case. For this left corner the inner wheel(left wheel) is limiting the torque, and therefore the torque vectoring torque for TV(1). The limiting factor for TV(0) is the drive torque constraint, which is now more significant then in the previous run.

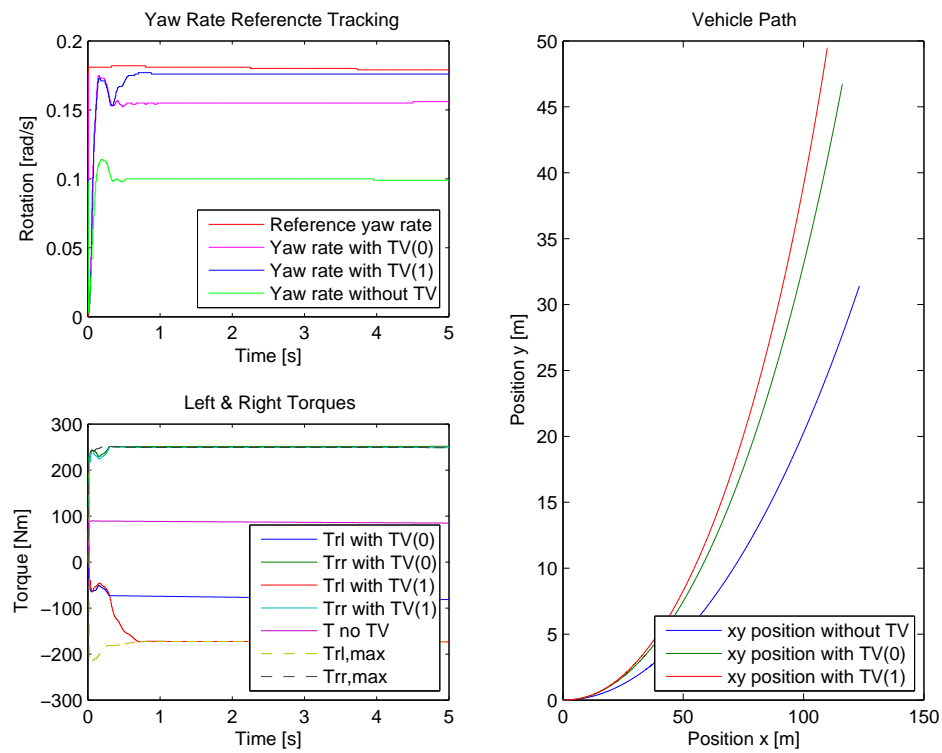


Figure 6-5: Plot of the yaw rate tracking, torques and vehicle path for a constant steer input of 10°

6-3 180° turn

In this simulation there is a fixed corner of 180°. The simulation of this turn is executed three times, with and without torque vectoring; TV(0) and TV(1). The goal is to achieve the highest possible velocity without driving outside the corner. In all three runs the steering angle is 30 degrees and the initial velocity is equal to the exit velocity. The throttle is scaled to the velocity and therefore differs for all three runs. In all the runs the buffer capacity is included in the total power of the vehicle, so the vehicle runs on full power.

The first run is performed without torque vectoring. When no torque vectoring is applied the maximum velocity is only 45 km h⁻¹. The path of the vehicle starts in the middle of the road but after the corner diverges to the outer side of the road. For TV(0) the maximum velocity is 75 km h⁻¹ which is significantly higher than when no torque vectoring was applied. The path for TV(0) is much wider and closer to the outer side of the road than when no torque vectoring was used. This is mainly due to the higher velocity which pushed the vehicle to the outer side. For TV(1) the maximum velocity is 72 km h⁻¹ which is lower than the velocity of TV(0). This can be explained by the fact that TV(1) is not maintaining the demanded drive torque, where is done in TV(0). TV(1) gives the priority to the torque vectoring torque, which explains the much tighter path through the corner. Where TV(0) drives along the outer side, TV(1) drives along the inner side of the road.

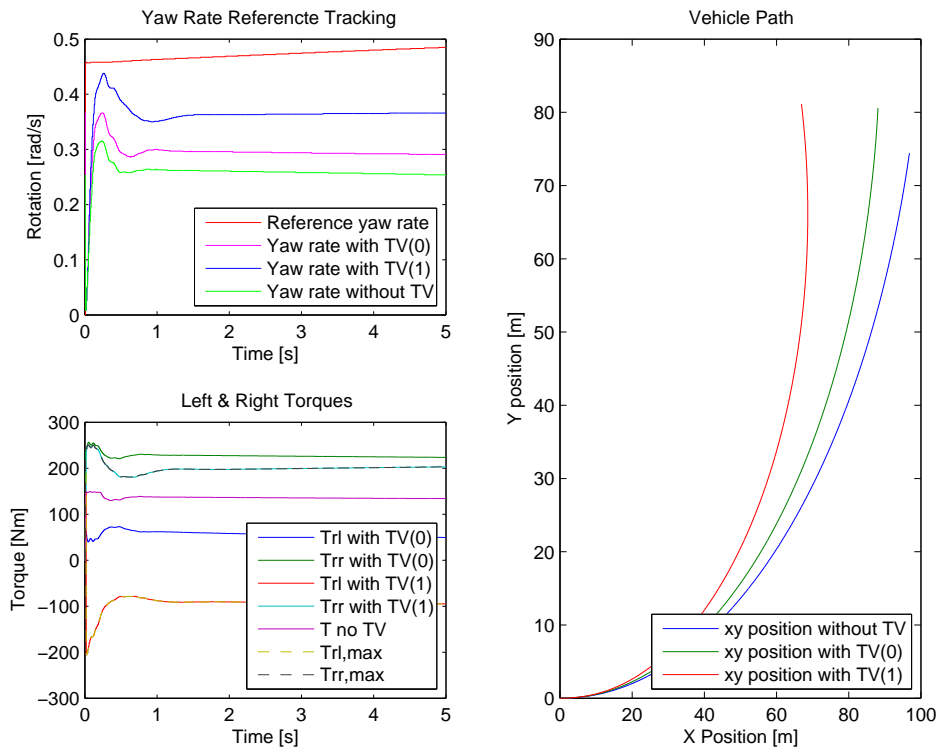


Figure 6-6: Plot of the yaw rate tracking, torques and vehicle path for a constant steer input of 30°

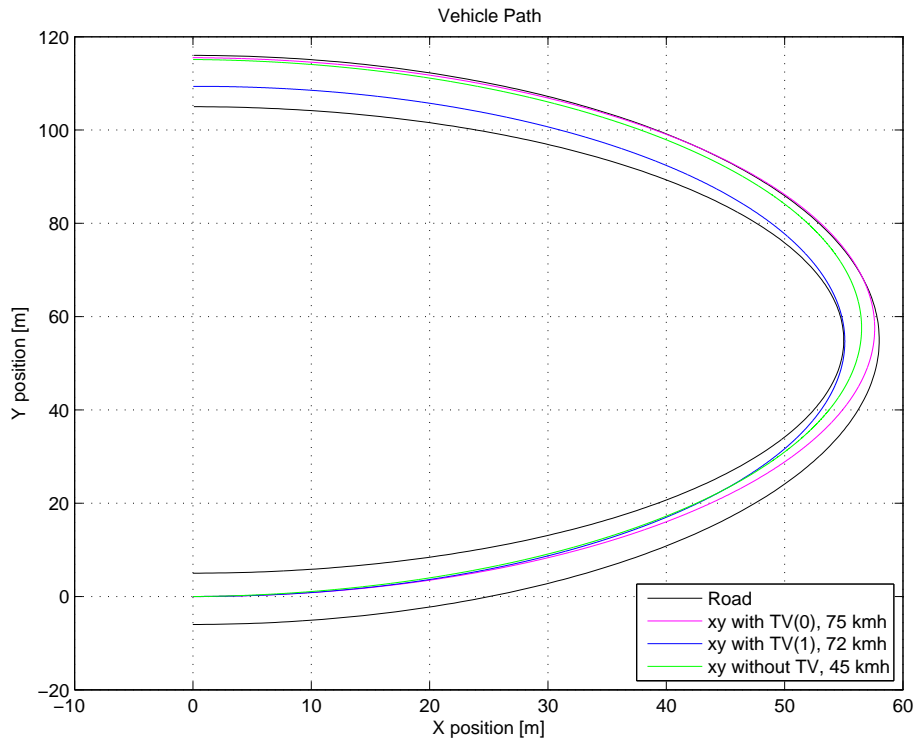


Figure 6-7: Plot of the vehicle paths for a 180° turn

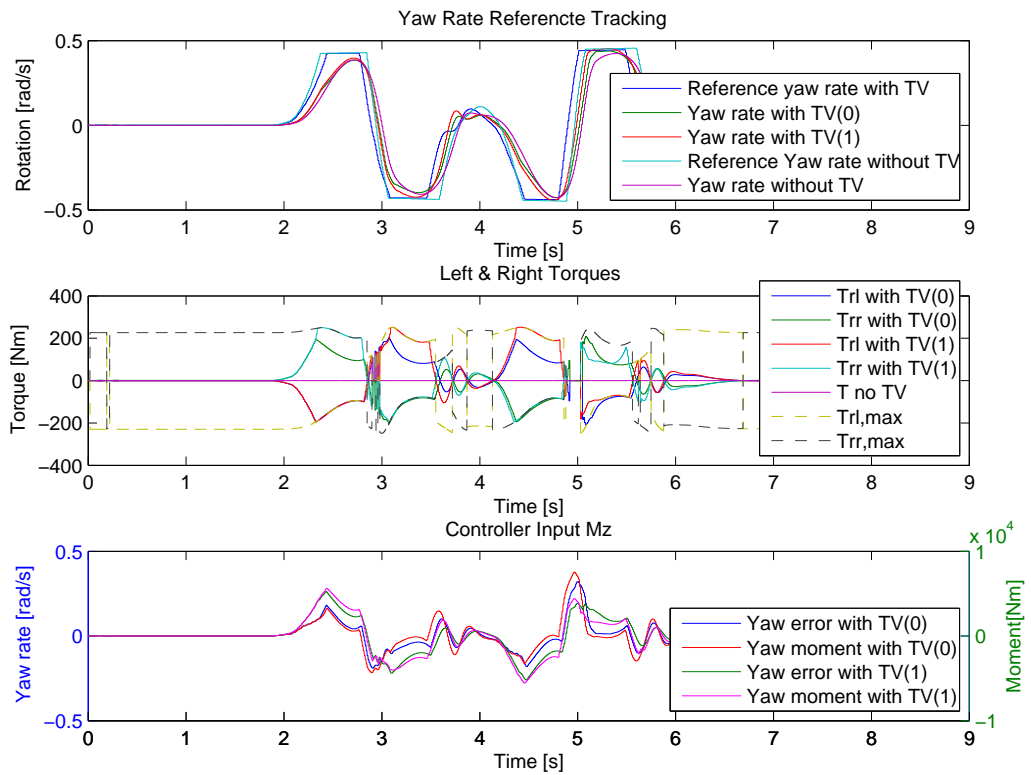


Figure 6-8: Plot of the yaw rate tracking, controller in/output and torques for a double lane change

6-4 Double lane change

In this simulation a double lane change is performed on the vehicle to simulate quick corner behavior. In this test the vehicle will begin with an initial velocity of 100 km h^{-1} without throttle input. During the run the vehicle tries to follow the ideal path through the double lane change. The cornering test is executed 3 times, with and without torque vectoring; TV(0) and TV(1). In all the runs the buffer capacity is included in the total power of the vehicle, so the vehicle runs on full power. The first run is executed with the vehicle without torque vectoring. In this run the exit velocity is 87.21 km h^{-1} . The run with no torque vectoring has a relatively large overshoot, compared to the runs with torque vectoring, even though the velocity is lower. The second run is with TV(0) and shows a path with a smaller overshoot, this means that the cornering behavior is improved. The vehicle is now capable of taking a corner with a smaller radius. The exit velocity of TV(0) is 87.49 km h^{-1} . This is a small difference with the exit velocity of the run with no torque vectoring. There is a large decrease in the overshoot. For TV(1) the exit velocity is 89.06 km h^{-1} which is a more significant increase with respect to no torque vectoring. For TV(1) the overshoot is about same as for TV(0), but with a higher exit velocity. This can be explained by the fact that for TV(1) only the torque limitation of the friction circle, and not the equality constraint of the drive torque is considered. This means that the torque vectoring torque can be larger, and therefore

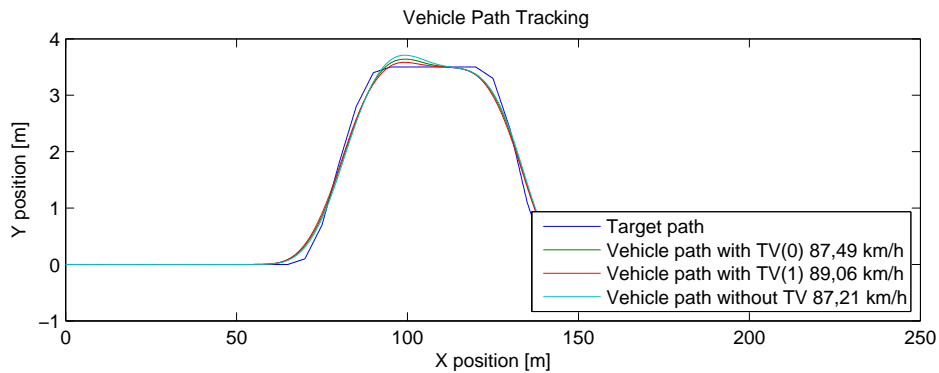


Figure 6-9: Plot of the vehicle path for a double lane change

the cornering behavior is better. This is confirmed in the the second sub plot shown in Figure 6-9. This figure shows the total drive torque in for TV(0) and TV(1). It is clear that the drive for TV(1) is not zero for the whole run. This means that the run with TV(1) consummates energy, and TV(0) not. This means that the greater performance of TV(1) comes at the cost of consummating energy.

6-5 Conclusion

Looking at the four different test procedures, it is clear that torque vectoring has an effect on the vehicle's behavior. When torque vectoring is used the lateral behavior of the vehicle improves and leads to higher velocities when corners are taken. This improve in velocity can lead to faster lap times, as the vehicle will leave the corner with a higher velocity then it would have when no torque vectoring was applied. The difference between $\kappa = 0$ and $\kappa = 1$ are also clearly noticeable. With $\kappa = 0$ the vehicle is performing in most simulation not as good as the when $\kappa = 1$, but is much better when no torque vectoring is used. The upside of $\kappa = 0$ is that the drive torque is still proportional to the gas pedal at all times. The driver will not notice a loss in drive torque and therefore $\kappa = 0$ will have less impact on the drivers experience. The downside is that with $\kappa = 0$ the vehicle will perform less in quick handling maneuvers and where the smallest corner radius is desired. The downside of $\kappa = 1$ is that the driver will notice the decrease in drive torque even though he might want to increase this drive torque. The driver is therefore no longer in control over the acceleration of the vehicle. How this will effect the performance needs to be determined in a real time simulation with a physical driver.

The PI and LP controller shows an increase in the lateral performance compared to the non torque vectoring case. The expectation is that with a non-linear controller the performance can even more increase. With a more comprehensive vehicle and tire model the dynamic behavior can be determined with greater accuracy. This should improve the control action, and lead to better performance. Furthermore, this control algorithm is only capable of determining the torques for the rear wheels. Controlling all four wheel with this control algorithm is not a possibility. Therefore, in the next

chapter a second controller will be presented that is based upon non-linear vehicle and tire models, which can be used on an All Wheel Drive (AWD) vehicle.

Chapter 7

LP Controller

In this chapter the second control method for torque vectoring will be presented. This controller is a follow up on the first controller. To improve the performance of the first controller there is chosen to replace the linear models used in the first controller with non-linear models. This means that the linear bicycle model will be replaced with a non-linear two track model. This will give the opportunity to use this controller when Forze will develop a vehicle with All Wheel Drive (AWD). The tire model is also no longer linear. The lateral force will be determined with the use of the slip angle, slip ratio and wheel loads. The new controller is based upon Linear Programming (LP), see Figure 7-1. In the first section the new control method will be presented and explained. The second section will give the necessary models for this new control method. The last section will show the constraints needed for this new torque vectoring control method. The constraint used in this LPcontroller are all torque position related. There are no constraints considered for the the torque rate.

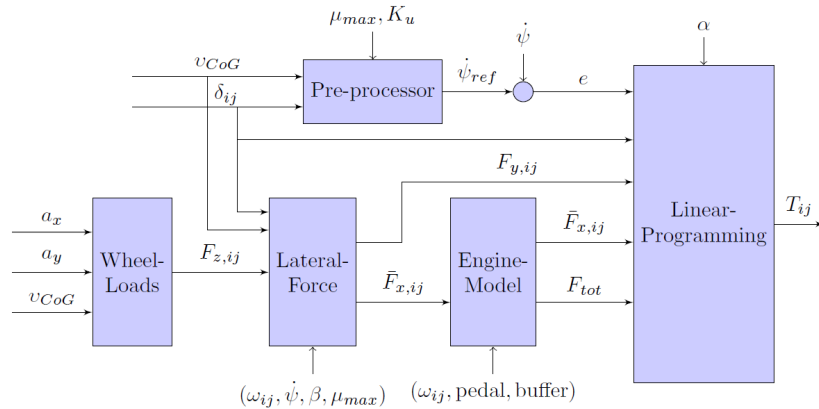


Figure 7-1: LP control setup

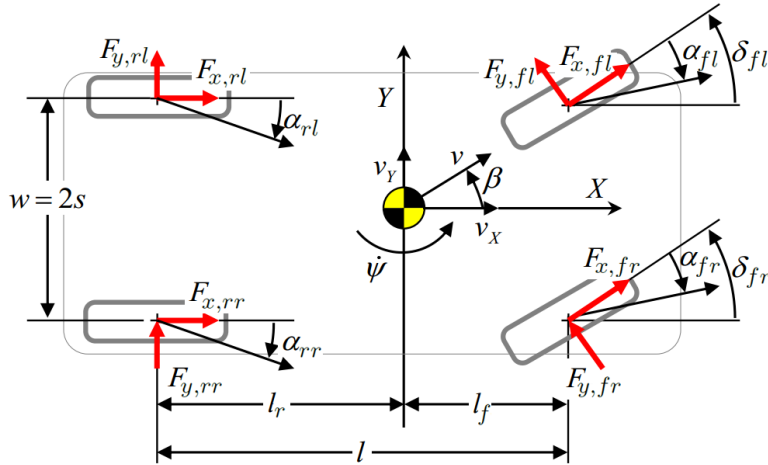


Figure 7-2: Two-track vehicle model [5]

7-1 Control algorithm

The new control method is based upon a two-track vehicle model. The two-track model is mostly used when all wheel forces are individually controllable. In case of the Forze VI, only the rear wheels are controllable. However, the future Forze will probably have a AWD racing vehicle. This model will then also be suitable for future racing vehicles. In the two-track model all wheels will be modeled separately and therefore the effect of the differences in the longitudinal forces on the yaw motion will be considered in the model. A schematic representation of the two-track model can be seen in Figure 7-2. In this figure all individual wheel forces and directions are shown. The location for the longitudinal velocity v_x , the lateral velocity v_y , and the yaw rate $\dot{\psi}$ is at the Center of Gravity (CoG). The figure shows the steering angle δ and the slip angles α_{ij} where i and j are indicating the front/rear axle and the left/right side of the vehicle.

It is assumed that the left and right front wheel turn angles are of the same magnitude, hence $\delta_{fl} \approx \delta_{fr} \approx \delta$. Further it is assumed that the left and right rear wheel turn angle are not of any significance, hence $\delta_{rl} \approx \delta_{rr} \approx 0$.

Equation's of Motions

From newton's second law of motion the equation's of motion for motion in the longitudinal, lateral, and yaw direction are:

$$\begin{aligned} Ma_x &= (F_{x,fl} + F_{x,fr}) \cos \delta - (F_{y,fl} + F_{y,fr}) \sin \delta + F_{x,rl} + F_{x,rr} \\ Ma_y &= (F_{x,fl} + F_{x,fr}) \sin \delta - (F_{y,fl} + F_{y,fr}) \cos \delta + F_{y,rl} + F_{y,rr} \\ J_z \ddot{\psi} &= -s_f(F_{x,fl} - F_{x,fr}) \cos \delta - \ell_f(F_{x,fl} + F_{x,fr}) \sin \delta - s_r(F_{x,rl} - F_{x,rr}) \\ &\quad + s_f(F_{y,fl} - F_{y,fr}) \sin \delta + \ell_f(F_{y,fl} + F_{y,fr}) \cos \delta - \ell_r(F_{y,rl} + F_{y,rr}) \end{aligned} \quad (7-1)$$

This new controller will be a yaw rate tracking controller just like the previous controller. Because it will only be a yaw rate tracking controller the equation's of motion

for the lateral en longitudinal motion can be neglected. The reason for neglecting the lateral and longitudinal motion equations is that only the yaw rate will be controlled, and therefore only the rotational motion equation is required. The equation's of motion for the LP control method can be reduced to only the following equation of motion:

$$\begin{aligned} J_z \ddot{\psi} = & -s_f(F_{x,fl} - F_{x,fr}) \cos \delta - \ell_f(F_{x,fl} + F_{x,fr}) \sin \delta - s_r(F_{x,rl} - F_{x,rr}) \\ & + s_f(F_{y,fl} - F_{y,fr}) \sin \delta + \ell_f(F_{y,fl} + F_{y,fr}) \cos \delta - \ell_r(F_{y,rl} + F_{y,rr}) \end{aligned} \quad (7-2)$$

In this control method the longitudinal force $F_{x,ij}$ will be the control output and the control input is the yaw rate error $\dot{\psi}$, see Equation 7-5. The equation of motion for the motion of yaw can be reformulated. This will be done by collecting all the constant and known values in one constant and constructing a constant vector for the control inputs. Whit this reformulation a distinction is made between the states and the constants:

$$\ddot{\psi} = \vec{K}_1 F_{x,ij} + K_2 \quad (7-3)$$

with:

$$\begin{aligned} \vec{K}_1 &= \frac{1}{J_z} \begin{bmatrix} -s_f \cos \delta + \ell_f \sin \delta \\ s_f \cos \delta + \ell_f \sin \delta \\ -s_r \\ s_r \end{bmatrix}^T \\ K_2 &= \frac{1}{J_z} (s_f(F_{y,fl} - F_{y,fr}) \sin \delta + \ell_f(F_{y,fl} + F_{y,fr}) \cos \delta - \ell_r(F_{y,rl} + F_{y,rr})) \end{aligned} \quad (7-4)$$

In this new formulation of the equation's of motion a constant vector \vec{K}_1 and a constant K_2 are introduced. Vector \vec{K}_1 consist of vehicle constants and vehicle parameters. The vehicle parameter δ will be determined with a model of the steering system in the Forze VI, this model is the same steering model as presented in Section 5-1-3. The constant K_2 consist of the same constants and vehicle parameters as \vec{K}_1 , but also includes the lateral wheel forces. Section 7-2 will present a model which determines the lateral wheel forces.

The goal of the LP controller is to achieve the smallest yaw rate error between the actual yaw rate and the reference yaw rate from the reference generator. The reference yaw rate $\dot{\psi}_{ref}$ is generated by the same reference generator used in Chapter 5. The yaw error $\dot{\psi}$ is determined with the following equation:

$$\dot{\psi} = \dot{\psi}_{ref} - \dot{\psi} \quad (7-5)$$

The control method in Chapter 5 consist of three different sections: pre-processor, controller and post-processor. The control method in this chapter will consist of only two different sections: pre-processor and controller. This new controller is a combination of the controller and post-processor of the previous control method. The Proportional

Integral (PI) controller is now integrated into the post-processor. The PI controller part can now be described as:

$$\ddot{\psi} = K_p \dot{\psi} + K_i \int \dot{\psi} dt \quad (7-6)$$

Combining Equation's 7-3, 7-5 and 7-6 the following relation for the control is found:

$$\ddot{\psi} = \vec{K}_1 F_X + K_2 = K_p \dot{\psi} + K_i \int \dot{\psi} dt \quad (7-7)$$

In this relation both the controller input and output are present. There is now a relation between the longitudinal forces (states) and the yaw rate error. When a yaw rate error occurs the system will steer towards the desired yaw such that the yaw error goes to zero. The settling time is determined by the value of K_p and K_i . The values for K_p and K_i are chosen such that the overshoot and settling time are minimized. The values for K_p and K_i are presented in the Table 7-1

Table 7-1: PI values

K_p	40
K_i	3

In this LP problem the longitudinal forces are constraint by the same constraints $\bar{F}_{x,ij}$ used in the first controller, see Chapter 5. The goal of this LP problem is not to ensure the desired yaw moment M_z from the PI controller, but to achieve the desired yaw rate $\dot{\psi}_{ref}$. Achieving the desired yaw rate is performed while maximizing the total amount of driving torque on the road. This way the LP controller ensures the largest possible drive torque while tracking the desired yaw rate.

$$\begin{aligned} \min_{F_{x,ij}} \quad & \bar{F}_{x,ij} - F_{x,ij} \\ \text{subject to} \quad & \vec{K}_1 F_{x,ij} = -K_2 + K_p \dot{\psi} + K_i \int \dot{\psi} dt \\ & F_{x,ij} \leq \bar{F}_{x,ij} \\ & F_{x,ij} \geq -\bar{F}_{x,ij} \\ & \sum F_{x,ij} \leq F_{tot} \end{aligned}$$

At some point it is not possible to maintain a certain yaw tracking performance due to the fact that the tire limits are reached and the torque vectoring torque no longer can increase. This means that the linear control problem becomes infeasible. This needs to be prevented at all time, as this will give invalid torque outputs. To prevent this an exact penalty function ϵ is introduced. This exact penalty function will be added to the constraint of the yaw tracking. This means when the longitudinal forces of the tires are at the limit of their friction circles, the performance of the tracking will decrease and the exact penalty function will increase to ensure the linear problem to maintain

feasible. This means that the yaw error will increase but the longitudinal forces keep inside the friction circles.

$$\begin{aligned} \min_{F_{x,ij}} \quad & \bar{F}_{x,ij} - F_{x,ij} + \epsilon \\ \text{subject to} \quad & \vec{K}_1 F_{x,ij} = -K_2 + K_p \dot{\psi} + K_i \int \dot{\psi} dt + \epsilon \\ & F_{x,ij} \leq \bar{F}_{x,ij} \\ & F_{x,ij} \geq -\bar{F}_{x,ij} \\ & \sum F_{x,ij} \leq F_{tot} \\ & \epsilon \geq 0 \end{aligned}$$

Implementing this linear programming problem in LabVIEW in this particular form is not possible. The solver of the linear programming problem does not allow negative values in the solution vector. This would mean that the values of the longitudinal forces never could become negative, although this certainly could be a valid solution. A solution to this problem is to introduce a change of coordinates, such that lowest possible solution is zero. This is done by adding a slack variable. This slack variable is chosen to be value of the largest possible constraint, which is 400 N m coming from the engine constraints.

$$\tilde{F}_{x,ij} = F_{x,ij} + \vec{F}_{sv} \quad (7-8)$$

This means that the linear programming problem needs to be adapted as follows:

$$\begin{aligned} \min_{\tilde{F}_{x,ij}} \quad & \bar{F}_{x,ij} - \tilde{F}_{x,ij} + \vec{F}_{sv} + \epsilon \\ \text{subject to} \quad & \vec{K}_1 \tilde{F}_{x,ij} = -K_2 + K_p \dot{\psi} + K_i \int \dot{\psi} dt + \vec{K}_1 \vec{F}_{sv} + \epsilon \\ & \tilde{F}_{x,ij} \leq \bar{F}_{x,ij} + \vec{F}_{sv} \\ & \tilde{F}_{x,ij} \geq -\bar{F}_{x,ij} + \vec{F}_{sv} \\ & \sum \tilde{F}_{x,ij} \leq F_{tot} + 4\vec{F}_{sv} \\ & \epsilon \geq 0 \end{aligned}$$

The solution of the linear programming is now $\tilde{F}_{x,ij}$, which is always a positive value. But this is not the longitudinal forces for the wheels. To obtain the longitudinal forces the slack variable needs to be extracted. This way the linear programming problem will give a negative solution for the longitudinal forces:

$$F_{x,ij} = \tilde{F}_{x,ij} - \vec{F}_{sv} \quad (7-9)$$

7-2 Vehicle modeling

To use this new control method the vector constant \vec{K}_1 and the constant K_2 from Equation 7-4 needs to be known. The vehicle constants in the vector constant \vec{K}_1 are

already known as they are the same as for the first controller. The constant K_2 is not that easy to determine. To determine this constant the lateral forces are needed to be calculated. The calculation of this lateral force and all the other vehicle parameters for this calculation will be explained in this chapter.

7-2-1 Steering

In this subsection a model will be given which will be able to estimate the steering angle δ en the wheel slip angle α . This will be done with the use of the knowledge of the sensor data and with the information of the mechanical steering construction.

For this new control approach not only the front steering angles needs to be known, but also the rear steering angles. For the front wheels the relation for the dynamic toe is determined in Section 5-1-3. The dynamic toe is depended on the suspension jounce and the steering arm angle. For the rear wheel there is no steer arm angle, so for the rear wheels only the suspension jounce is considered. To determine the dynamic toe relation for the rear wheels, only the effect of the wheel loads on the toe are considered. The relationship between the wheel loads and the toe angle, seems to be relatively linear. Therefore, a linear function is chosen to map the relationship between the rear wheel loads en the rear toe angles.

Table 7-2: Static toe

Wheel	Toe angle [deg]
Rear left	0.2
Rear right	0.2

With all the four steering angles δ_{ij} known, it is now possible to determine the slip angle α_{ij} of all four wheels. This will be done with the following relation from [7].

$$\begin{aligned}\alpha_{fl} &= -\beta + \delta_{fl} - \frac{\ell_f \cdot \dot{\psi}}{v_{CoG} - .5\dot{\psi} \cdot w_b} \\ \alpha_{fr} &= -\beta + \delta_{fr} - \frac{\ell_f \cdot \dot{\psi}}{v_{CoG} + .5\dot{\psi} \cdot w_b} \\ \alpha_{rl} &= -\beta + \delta_{rl} + \frac{\ell_r \cdot \dot{\psi}}{v_{CoG} - .5\dot{\psi} \cdot w_b} \\ \alpha_{rr} &= -\beta + \delta_{rr} + \frac{\ell_r \cdot \dot{\psi}}{v_{CoG} + .5\dot{\psi} \cdot w_b}\end{aligned}\tag{7-10}$$

7-2-2 Wheel velocities

In this section the lateral wheel forces will be determined. For the second control method it is important to know the lateral forces. This is because they will be used to determine the maximum allowable longitudinal forces. A well known method to determine these lateral force is the use of the magic tire formula from Hans B. Pacejka [8]. Unfortunately there are no Pacejka tire parameter available from the tires of the Forze

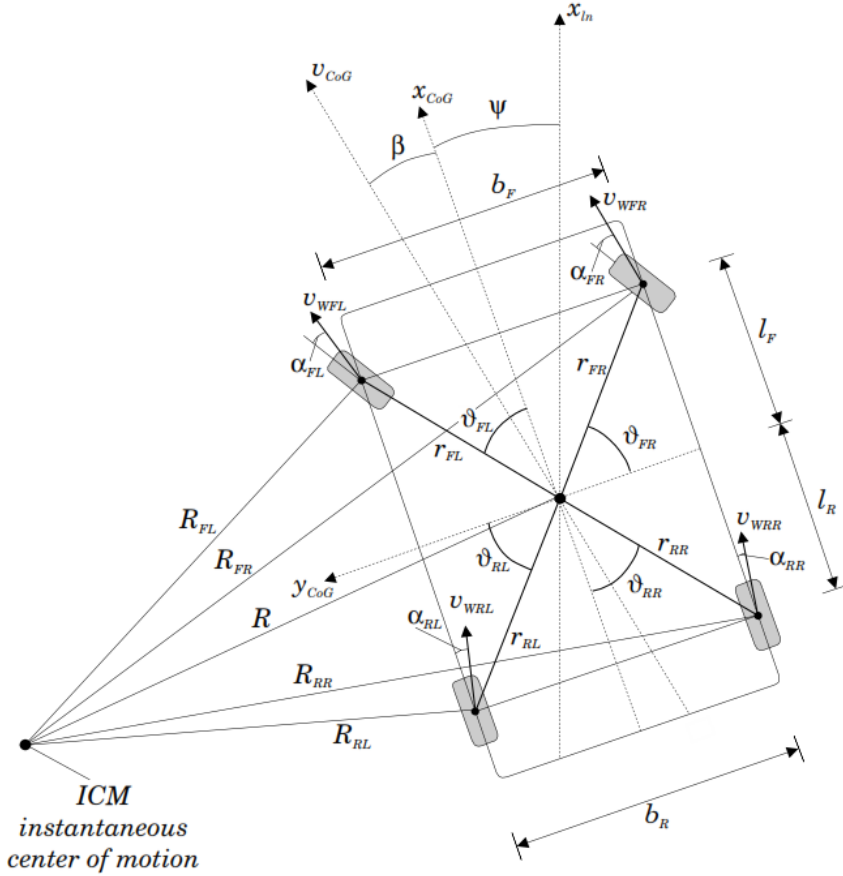


Figure 7-3: The curve radii of each individual wheel

VI, the use of a magic tire formula is therefore not a possibility. The only parameters that are known from the tires are the cornering stiffness C_{ij} and the maximum allowable slip-ratio $\lambda_{max,ij}$. In the book of Kiencke & Nielson [7] a method is proposed, where the lateral wheel forces can be determined with the use of only these parameters, see Section 7-2-4.

In this approach of Kiencke & Nielson [7] it is necessary to know the wheel slip λ_{ij} , tire side slip α_{ij} and the friction coefficient μ . To determine the individual wheel slip the individual wheel velocities needs to be determined. For the tire slip it is necessary to know the body slip angle β . The individual wheel slip is determined with the use of the wheel ground contact point velocity or wheel velocity $v_{W,ij}$ and the rotational equivalent velocity $v_{R,ij}$. A method to determine the wheel velocity is to obtain the vehicle movement as an orbit around the instantaneous center with angular velocity $\dot{\psi}$ and $\dot{\beta}$. With this information it is possible to calculate the curve radius to each individual wheel. For this method the distance from the CoG to the wheel-ground contact point needs to be known.

The velocities of the CoG and the wheel ground contact points are perpendicular to the connecting lines to the Instantaneous Center of Motion (ICM), as shown in Figure 7-

3. If the assumption is made that the distance R from the vehicle CoG to the ICM is much larger than the distances r_{ij} , the differential radii ΔR_{ij} can be considered as parallel lines. With this assumption it is possible to determine the wheel velocities $v_{W,ij}$ without knowing the absolute turn radius R of the CoG. Another made assumption is that the effect of the caster angles needs to be neglected. With these two assumptions the differential radii can be calculated using the following equations:

$$\begin{aligned}\Delta R_{fl} &= \frac{wb_f}{2} \cos \beta - \ell_f \cdot \sin \beta \\ \Delta R_{fr} &= \frac{wb_f}{2} \cos \beta + \ell_f \cdot \sin \beta \\ \Delta R_{rl} &= \frac{wb_r}{2} \cos \beta + \ell_r \cdot \sin \beta \\ \Delta R_{rr} &= \frac{wb_r}{2} \cos \beta - \ell_r \cdot \sin \beta\end{aligned}\tag{7-11}$$

The wheel velocities can now be calculated by using an additive superposition of the CoG velocity v_{CoG} and the additional angular velocity due to the distance ΔR_{ij} from the wheel to the center of gravity.

$$v_{W,ij} = v_{CoG} \mp \dot{\psi} \Delta R_{ij}\tag{7-12}$$

substituting Equation 7-12 gives:

$$\begin{aligned}v_{W,fl} &= v_{CoG} - \dot{\psi} \left(\frac{wb_f}{2} - \ell_f \beta \right) \\ v_{W,fr} &= v_{CoG} + \dot{\psi} \left(\frac{wb_f}{2} + \ell_f \beta \right) \\ v_{W,rl} &= v_{CoG} - \dot{\psi} \left(\frac{wb_r}{2} + \ell_r \beta \right) \\ v_{W,rr} &= v_{CoG} + \dot{\psi} \left(\frac{wb_r}{2} - \ell_r \beta \right)\end{aligned}\tag{7-13}$$

The next step is to determine the rotational equivalent wheel velocity $v_{R,ij}$. This is done with the use of the following equations:

$$\begin{aligned}v_{R,fl} &= \omega_{fl} \cdot r_{stat,f} \\ v_{R,fr} &= \omega_{fr} \cdot r_{stat,f} \\ v_{R,rl} &= \omega_{rl} \cdot r_{stat,r} \\ v_{R,rr} &= \omega_{rr} \cdot r_{stat,r}\end{aligned}\tag{7-14}$$

7-2-3 Wheel slip

Besides the wheel velocity $v_{W,ij}$ and the rotational equivalent wheel velocity $v_{R,ij}$, the tire side slip is also required to determine the wheel in lateral s_s en longitudinal s_l

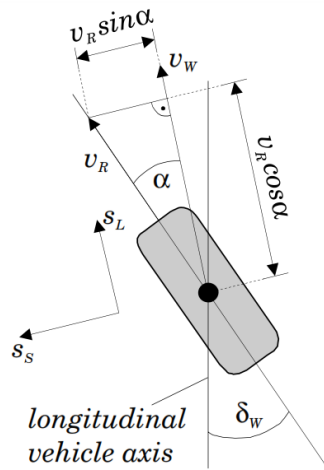


Figure 7-4: Wheel model for slip calculations

direction. That is because the wheel slip is a vector and thus the velocities in the slip direction must be transformed, see Figure 7-4.

If the vehicle drives without tire side slip, the wheel slip is simply the difference between the rotational equivalent wheel velocity $v_{R,ij}$ and the CoG velocity v_{CoG} . In the approach of Kiencke & Nielson [7] there is chosen to use the method of Burckhardt [9] for calculating the longitudinal and lateral slip. Burckhardt calculates the longitudinal wheel slip in the direction of motion of the wheel, as well as the force. Hence the longitudinal slip s_l is defined in the direction of the wheel velocity $v_{W,ij}$ and the lateral slip s_s perpendicular to the wheel velocity $v_{W,ij}$. The wheel slip always needs to be between -1 and 1 and therefore the speed difference is divided by the respective larger speed, hence v_W for braking and $v_{R,ij}$ for driving. So for braking the slip is calculated

as follows:

$$\begin{aligned}
 s_{l,fl} &= \frac{v_{R,fl} \cos \alpha_{fl} - v_{W,fl}}{v_{W,fl}} \\
 s_{s,fl} &= \frac{v_{R,fl} \sin \alpha_{fl}}{v_{W,fl}} \\
 s_{l,fr} &= \frac{v_{R,fr} \cos \alpha_{fr} - v_{W,fr}}{v_{W,fr}} \\
 s_{s,fr} &= \frac{v_{R,fr} \sin \alpha_{fr}}{v_{W,fr}} \\
 s_{l,rl} &= \frac{v_{R,rl} \cos \alpha_{rl} - v_{W,rl}}{v_{W,rl}} \\
 s_{s,rl} &= \frac{v_{R,rl} \sin \alpha_{rl}}{v_{W,rl}} \\
 s_{l,rr} &= \frac{v_{R,rr} \cos \alpha_{rr} - v_{W,rr}}{v_{W,rr}} \\
 s_{s,rr} &= \frac{v_{R,rr} \sin \alpha_{rr}}{v_{W,rr}}
 \end{aligned} \tag{7-15}$$

and for driving:

$$\begin{aligned}
 s_{l,fl} &= \frac{v_{R,fl} \cos \alpha_{fl} - v_{W,fl}}{v_{R,fl} \cos \alpha_{fl}} \\
 s_{s,fl} &= \tan \alpha_{fl} \\
 s_{l,fr} &= \frac{v_{R,fr} \cos \alpha_{fr} - v_{W,fr}}{v_{R,fr} \cos \alpha_{fr}} \\
 s_{s,fr} &= \tan \alpha_{fr} \\
 s_{l,rl} &= \frac{v_{R,rl} \cos \alpha_{rl} - v_{W,rl}}{v_{R,rl} \cos \alpha_{rl}} \\
 s_{s,rl} &= \tan \alpha_{rl} \\
 s_{l,rr} &= \frac{v_{R,rr} \cos \alpha_{rr} - v_{W,rr}}{v_{R,rr} \cos \alpha_{rr}} \\
 s_{s,rr} &= \tan \alpha_{rr}
 \end{aligned} \tag{7-16}$$

The resultant slip wheel slip is the geometrical sum of the longitudinal and lateral slip:

$$\begin{aligned}
 s_{r,fl} &= \sqrt{s_{l,fl}^2 + s_{s,fl}^2} \\
 s_{r,fr} &= \sqrt{s_{l,fr}^2 + s_{s,fr}^2} \\
 s_{r,rl} &= \sqrt{s_{l,rl}^2 + s_{s,rl}^2} \\
 s_{r,rr} &= \sqrt{s_{l,rr}^2 + s_{s,rr}^2}
 \end{aligned} \tag{7-17}$$

7-2-4 Friction coefficient

The friction or adhesion coefficient μ is defined as the ratio of the frictional force F_{fric} acting on the wheel and the wheel load F_z :

$$\mu = \frac{F_{fric}}{F_z} \quad (7-18)$$

This friction coefficient is not constant value. The friction coefficient is depended on the wheel slip and wheel angles and is also different for every wheel load. The Burckhardt [9] method is a relative simple formula that can describe the friction curve. With three different parameters the characteristic of the curve can be constructed:

$$\mu(s_r) = c_1 \cdot (1 - e^{-c_2 \cdot s_r}) - c_3 \cdot s_r \quad (7-19)$$

Because there is no detailed information for the tire load sensitivity of the tires from Forze VI, only one curve will be used. This curve will be constructed with the Burckhardt curve using the information which is known from the tires. The cornering stiffness is found by calculating the slope of the tire curve. The Forze VI has different tires for the front and the rear, therefore the cornering stiffness is also different, see Table 7-3.

Table 7-3: Tire data

Tire	Cornering stiffness [N/rad]	μ_{max}
Front	$3.4698e + 04$	1.15
Rear	$5.2861e + 04$	1.17

With this tire data the following Burckhardt curves are constructed, see Figure 7-5. This curve is plotted with the following parameters set presented in Table 7-4. The

Table 7-4: Parameter set of the Burckhardt curves

Tire	c_1	c_2	c_3
Front	1.26	30	0.52
Rear	1.31	15	0.52

resultant slip s_{res} is directed in the same direction as the resultant friction coefficient μ_{res} . Hence the longitudinal and lateral friction coefficient can be calculated with the following equations:

$$\begin{aligned} \mu_{l,fl} &= \mu_{r,fl} \frac{s_{l,fl}}{s_{r,fl}} \\ \mu_{l,fr} &= \mu_{r,fr} \frac{s_{l,fr}}{s_{r,fr}} \\ \mu_{l,rl} &= \mu_{r,rl} \frac{s_{l,rl}}{s_{r,rl}} \\ \mu_{l,rr} &= \mu_{r,rr} \frac{s_{l,rr}}{s_{r,rr}} \end{aligned} \quad (7-20)$$

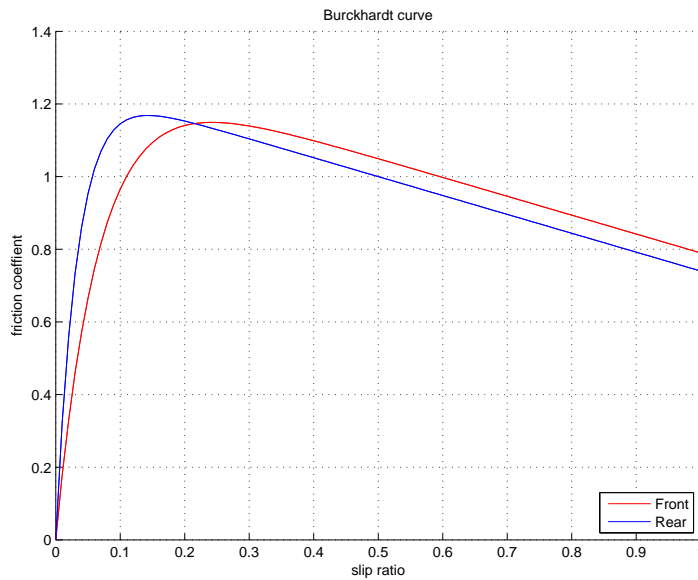


Figure 7-5: Plot of Burckhardt curves for the front and rear tires

$$\begin{aligned}
 \mu_{s,fl} &= \mu_{r,fl} \frac{s_{s,fl}}{s_{r,fl}} \\
 \mu_{s,fr} &= \mu_{r,fr} \frac{s_{s,fr}}{s_{r,fr}} \\
 \mu_{s,rl} &= \mu_{r,rl} \frac{s_{s,rl}}{s_{r,rl}} \\
 \mu_{s,rr} &= \mu_{r,rr} \frac{s_{s,rr}}{s_{r,rr}}
 \end{aligned} \tag{7-21}$$

If the assumption is made that the the friction behavior of the tire is independent of the direction of the slip, the behavior in Equations 7-21 & 7-22 can be described using a Kamm circle, see Figure 7-6. The Kamm circle assumes that the friction circle is a perfect circle, but in reality this is an ellipse. Using the information of the contact between tire and road, the velocity of the vehicle and the wheel loads, the level of the maximum resultant friction coefficient $\mu_{rmax,ij}$ can be calculated.

7-2-5 Lateral forces

Before the lateral and longitudinal forces can be calculated the friction force of the tires needs to be determined. The longitudinal friction force $F_{wl,ij}$ is determined in the direction of the wheel velocity v_w and the lateral friction force $F_{ws,ij}$ is determined in the direction orthogonal to the wheel velocity v_w . The frictional forces are calculated with the use of the wheel loads and the friction coefficients in lateral and longitudinal

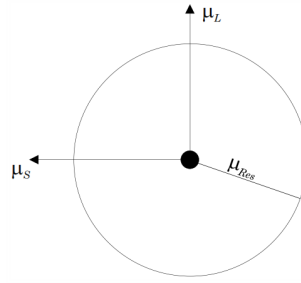


Figure 7-6: Kamm Circle

direction. In the longitudinal direction the frictional forces are:

$$\begin{aligned} F_{wl,fl} &= \mu_{l,fl} F_{z,fl} \\ F_{wl,fr} &= \mu_{l,fr} F_{z,fr} \\ F_{wl,rl} &= \mu_{l,rl} F_{z,rl} \\ F_{wl,rr} &= \mu_{l,rr} F_{z,rr} \end{aligned} \quad (7-22)$$

In the lateral direction the frictional forces are:

$$\begin{aligned} F_{ws,fl} &= \mu_{s,fl} F_{z,fl} \\ F_{ws,fr} &= \mu_{s,fr} F_{z,fr} \\ F_{ws,rl} &= \mu_{s,rl} F_{z,rl} \\ F_{ws,rr} &= \mu_{s,rr} F_{z,rr} \end{aligned} \quad (7-23)$$

These friction are now in the direction of the wheel velocity v_w and need to be transformed into the wheel coordinate system:

$$\begin{aligned} F_{l,fl} &= F_{wl,fl} \cos \alpha_{fl} + F_{ws,fl} \sin \alpha_{fl} \\ F_{l,fr} &= F_{wl,fr} \cos \alpha_{fr} + F_{ws,fr} \sin \alpha_{fr} \\ F_{l,rl} &= F_{wl,rl} \cos \alpha_{rl} + F_{ws,rl} \sin \alpha_{rl} \\ F_{l,rr} &= F_{wl,rr} \cos \alpha_{rr} + F_{ws,rr} \sin \alpha_{rr} \end{aligned} \quad (7-24)$$

$$\begin{aligned} F_{s,fl} &= F_{ws,fl} \cos \alpha_{fl} - F_{wl,fl} \sin \alpha_{fl} \\ F_{s,fr} &= F_{ws,fr} \cos \alpha_{fr} - F_{wl,fr} \sin \alpha_{fr} \\ F_{s,rl} &= F_{ws,rl} \cos \alpha_{rl} - F_{wl,rl} \sin \alpha_{rl} \\ F_{s,rr} &= F_{ws,rr} \cos \alpha_{rr} - F_{wl,rr} \sin \alpha_{rr} \end{aligned} \quad (7-25)$$

The longitudinal and side friction forces F_l and F_s needs to be transformed to the undercarriage coordinate system. Because the rear wheels of the Forze VI also have a

steering angle δ , they cannot be neglected. So for the translation all four steering angle are considered:

$$\begin{aligned} F_{y,fl} &= F_{s,fl} \cos \delta_{fl} + F_{l,fl} \sin \delta_{fl} \\ F_{y,fr} &= F_{s,fr} \cos \delta_{fr} + F_{l,fr} \sin \delta_{fr} \\ F_{y,rl} &= F_{s,rl} \cos \delta_{rl} + F_{l,rl} \sin \delta_{rl} \\ F_{y,rr} &= F_{s,rr} \cos \delta_{rr} + F_{l,rr} \sin \delta_{rr} \end{aligned} \quad (7-26)$$

7-3 Constraints

Now that all the constants are determined the last step is to determine the longitudinal force constraints for the linear programming problem. In the previous sections the lateral wheel forces are determined. With these lateral wheel forces and the friction coefficient the longitudinal force, that lays within the friction circle, can be calculated. This will be done with the use of the Kamm circle. Which states that when the geometric sum of the longitudinal and lateral wheel forces lies within the Kamm circle the resultant tire force can be transmitted to the road [10]:

$$\sqrt{F_{wl,ij}^2 + F_{ws,ij}^2} \leq \mu_{r,ij} \cdot F_{z,ij} \quad (7-27)$$

When the maximum frictions coefficient is used instead of the resulting friction coefficient, the maximum longitudinal force can be determined. Reformulating Equation 7-27 and substituting the maximum friction coefficient, gives the following relation for the maximum longitudinal forces:

$$\begin{aligned} \bar{F}_{wl,fl} &= \sqrt{(\mu_{max,fl} \cdot F_{z,fl})^2 + F_{ws,fl}^2} \\ \bar{F}_{wl,fr} &= \sqrt{(\mu_{max,fr} \cdot F_{z,fr})^2 + F_{ws,fr}^2} \\ \bar{F}_{wl,rl} &= \sqrt{(\mu_{max,rl} \cdot F_{z,rl})^2 + F_{ws,rl}^2} \\ \bar{F}_{wl,rr} &= \sqrt{(\mu_{max,rr} \cdot F_{z,rr})^2 + F_{ws,rr}^2} \end{aligned} \quad (7-28)$$

These maximum longitudinal friction are now in the direction of the wheel velocity v_w and need to be transformed into the wheel coordinate system. For this translation the lateral wheel forces of the previous section are used:

$$\begin{aligned} \bar{F}_{l,fl} &= \bar{F}_{wl,fl} \cos \alpha_{fl} + F_{ws,fl} \sin \alpha_{fl} \\ \bar{F}_{l,fr} &= \bar{F}_{wl,fr} \cos \alpha_{fr} + F_{ws,fr} \sin \alpha_{fr} \\ \bar{F}_{l,rl} &= \bar{F}_{wl,rl} \cos \alpha_{rl} + F_{ws,rl} \sin \alpha_{rl} \\ \bar{F}_{l,rr} &= \bar{F}_{wl,rr} \cos \alpha_{rr} + F_{ws,rr} \sin \alpha_{rr} \end{aligned} \quad (7-29)$$

$$\begin{aligned}
 \bar{F}_{s,fl} &= F_{ws,fl} \cos \alpha_{fl} - \bar{F}_{wl,fl} \sin \alpha_{fl} \\
 \bar{F}_{s,fr} &= F_{ws,fr} \cos \alpha_{fr} - \bar{F}_{wl,fr} \sin \alpha_{fr} \\
 \bar{F}_{s,rl} &= F_{ws,rl} \cos \alpha_{rl} - \bar{F}_{wl,rl} \sin \alpha_{rl} \\
 \bar{F}_{s,rr} &= F_{ws,rr} \cos \alpha_{rr} - \bar{F}_{wl,rr} \sin \alpha_{rr}
 \end{aligned} \tag{7-30}$$

The longitudinal and side friction forces \bar{F}_l and \bar{F}_s needs to be transformed to the undercarriage coordinate system. Because the rear wheels of the Forze VI also have a steering angle δ , they cannot be neglected. So for the translation all four steering angle are considered:

$$\begin{aligned}
 \bar{F}_{x,fl} &= \bar{F}_{l,fl} \cos \delta_{fl} - \bar{F}_{s,fl} \sin \delta_{fl} \\
 \bar{F}_{x,fr} &= \bar{F}_{l,fr} \cos \delta_{fr} - \bar{F}_{s,fr} \sin \delta_{fr} \\
 \bar{F}_{x,rl} &= \bar{F}_{l,rl} \cos \delta_{rl} - \bar{F}_{s,rl} \sin \delta_{rl} \\
 \bar{F}_{x,rr} &= \bar{F}_{l,rr} \cos \delta_{rr} - \bar{F}_{s,rr} \sin \delta_{rr}
 \end{aligned} \tag{7-31}$$

Chapter 8

Results LP Controller

In this Chapter, the simulation results of the Linear Programming (LP) controller will be presented. In this Chapter 4 different simulations will be presented. All these simulation are done with the use of CarSim and LabVIEW. The commands come from CarSim and are simulated in a non real-time simulation in LabVIEW. Different pre-programmed maneuvers will be used in CarSim to show the vehicle behavior for the two different cases: no torque vectoring and with torque vectoring.

8-1 Step response

The first simulation is a step response test. In the first test the vehicle will begin with an initial velocity of 60 km h^{-1} which will be maintained the entire run. During the run a step on the steering wheel is set. The first step response test is executed for a steer input step of 10° . In the second test the vehicle will begin with an initial velocity of 80 km h^{-1} which will be maintained the entire run. During the run a step on the steering wheel is set. The first step response test is executed for a steer input step of 30° . In both runs the buffer capacity is included in the total power of the vehicle. This means that the vehicle runs on full power for the whole test procedure.

In Figure 8-1 and Figure 8-2 the simulation results of a 10 degrees steering step input are shown. In the first subplot the reference tracking is shown. When after 3 sec the steering input of 10 degrees occurs, the vehicle without torque vectoring is not capable of reaching the reference yaw rate. The vehicle with torque vectoring is capable of reaching the reference yaw rate. The settling time is 0.26 seconds and the overshoot is 9.2%. The steady state error when no torque vectoring is applied is 0.028, respectively 24%. When the values of the settling time and overshoot are compared with the linear step response values in Section 5-2 they do not match. The values of the non-linear simulation are much higher. An explanation is the role of the steering angle δ which

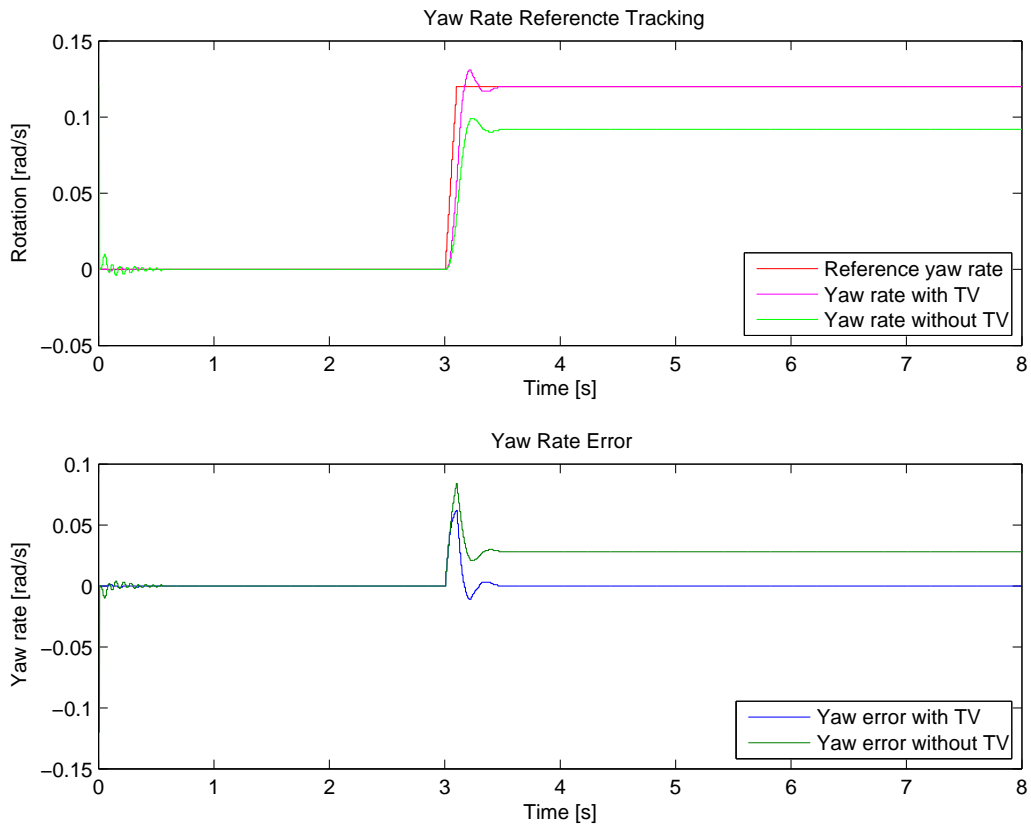


Figure 8-1: Plot of the yaw tracking and controller in/output for a step response of 10°

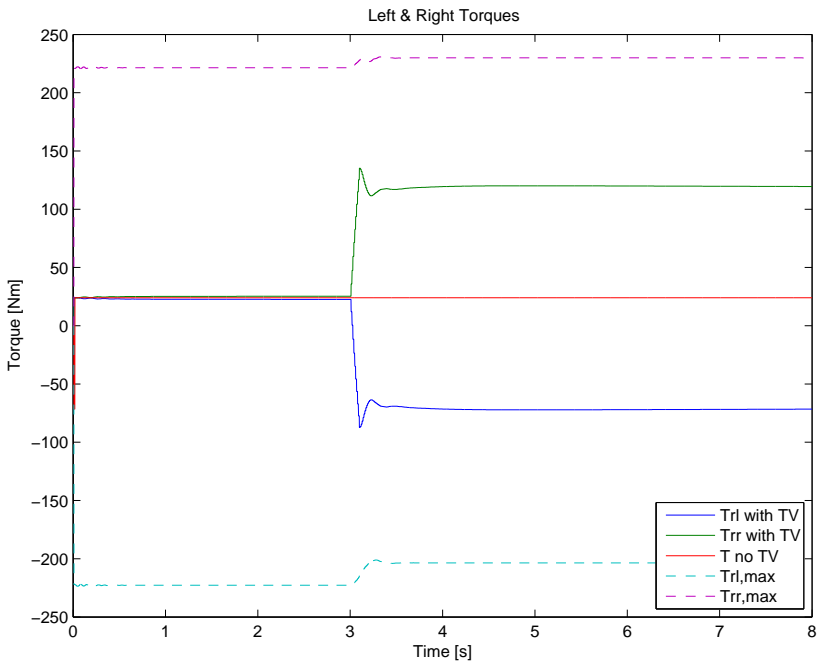


Figure 8-2: Plot of the torques for a step response of 10°

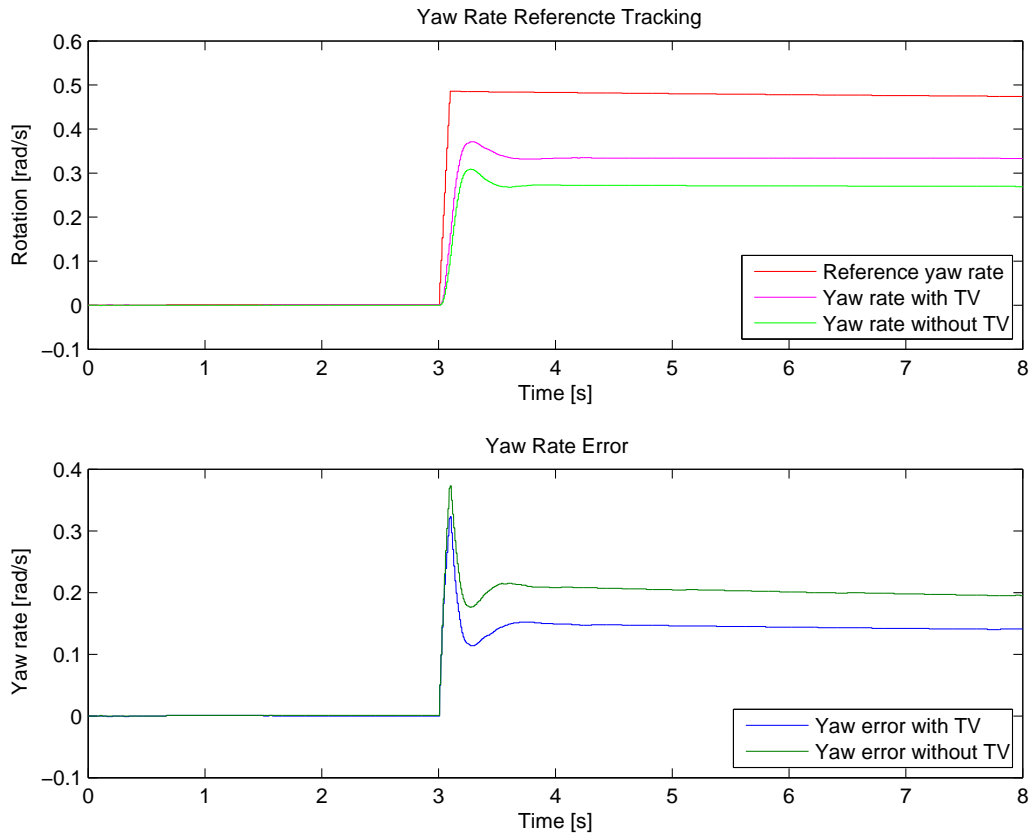


Figure 8-3: Plot of the yaw tracking and controller in/output for a step response of 30°

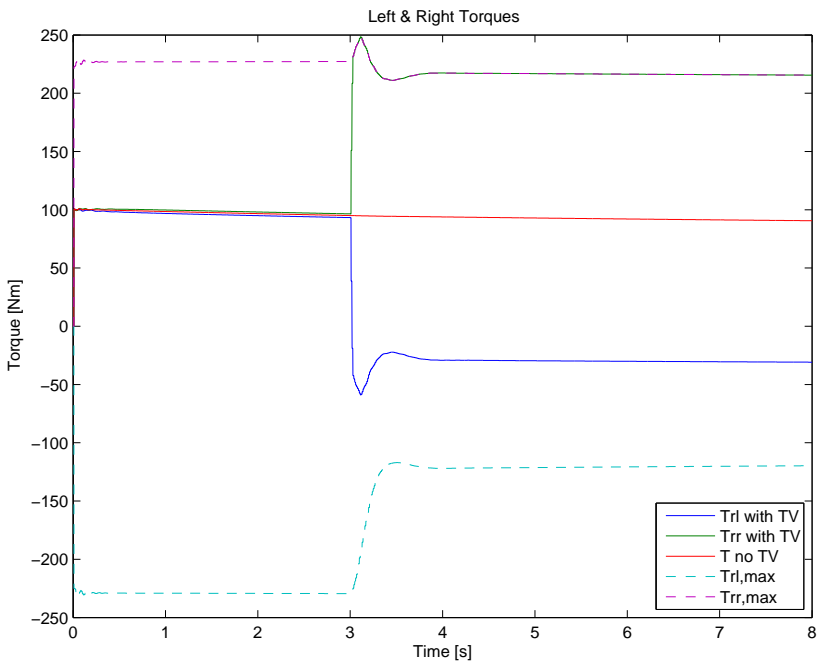


Figure 8-4: Plot of the torques for a step response of 30°

was neglected in the linear step response. Another explanation can be found in the non-linear effects of the real vehicle model and tire model.

In the other subplot the controller input(yaw error) is presented. For this simulation the yaw error with torque converges nicely to zero as the first subplot would suggest. Figure 8-2 shows that the demanded torque by the controller is within in the bounds of the maximum allowed torque from the slip controller.

In Figure 8-1 and Figure 8-2 the simulation results of a 30 degrees steering step input are presented. The first subplot shows the same characteristic of the vehicle without torque vectoring with a speed of 60 km h^{-1} and steering input of 10 degrees. For the vehicle with torque vectoring the yaw error no longer converges to zero. The reference signal can no longer be tracked perfectly which was the case in the first simulation. This is due to the fact that the demanded torques of the controller can no longer be reached. These torques are now restricted by the maximum allowed torques from the slip controller. The yaw rate can therefore no longer increase and reach the reference yaw rate.

8-2 Constant steer input

In this simulation a constant steering wheel input is set on the vehicle to simulate corner behavior. In this test the vehicle will begin with an initial velocity of 90 km h^{-1} which will be maintained the entire run. During the entire run the angle on the steering wheel is constant. The cornering test is executed 2 times for a constant steer input of 10° and 30° . In both runs the buffer capacity is included in the total power of the vehicle. This means that the vehicle runs on full power for the whole test procedure.

In Figure 8-5 the simulation results of a constant steering input of 10 degrees is shown. In the case of no torque vectoring the reference yaw rate can not be reached. This results in a smaller corner radius then the vehicle with torque vectoring. The vehicles with torque vectoring is also not capable of tracking the reference yaw rate. This due to the total drive torque constraint. Not all the torque vectoring torque potential is used. This simulation does shows the increase in lateral acceleration, or g force, generated by the torque vectoring torque.

In Figure 8-6 the simulation results of a constant steering input of 30 degrees is shown. In the case of no torque vectoring the reference yaw rate can again not be reached. For the vehicle with torque vectoring this is also the case. The limiting factor in this test is again the drive torque constraint, which is now more significant then in the previous simulation.

8-3 180° turn

In this simulation there is a fixed corner of 180° . The simulation of this turn is executed three times, with and without torque vectoring; TV(0) and TV(1). The goal is to

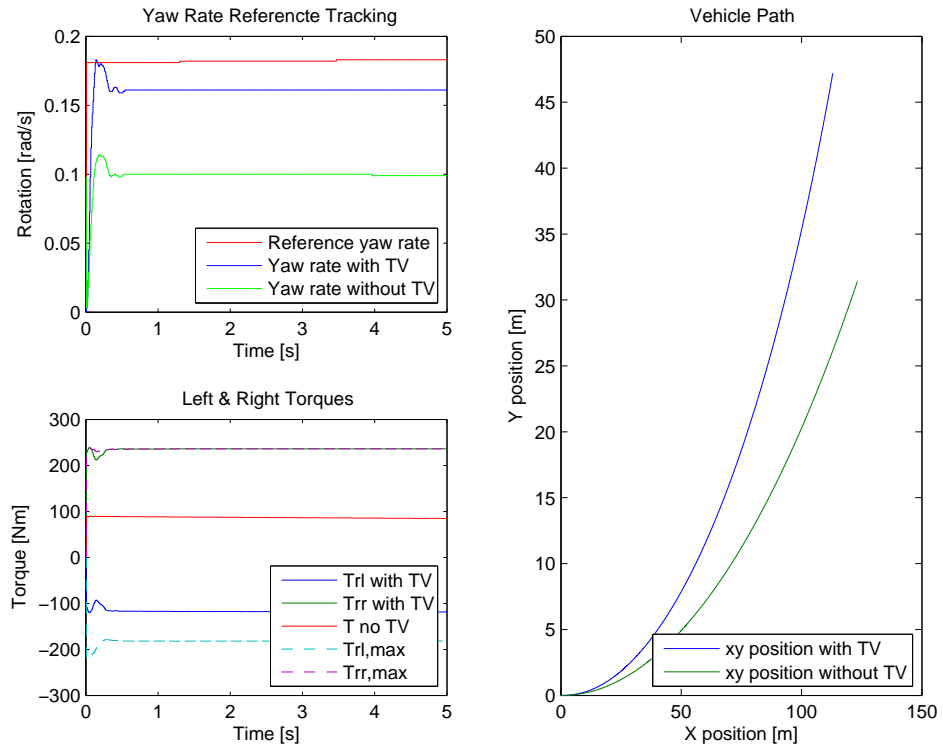


Figure 8-5: Plot of the yaw tracking, torques and vehicle path for a constant steer input of 10°

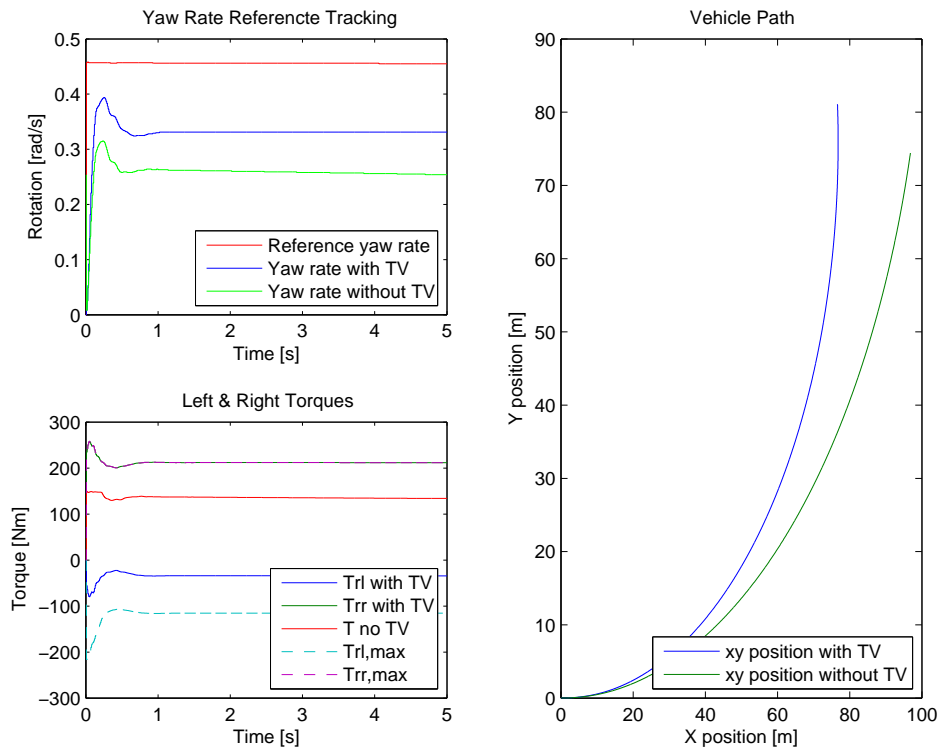


Figure 8-6: Plot of the yaw tracking, torques and vehicle path for a constant steer input of 30°

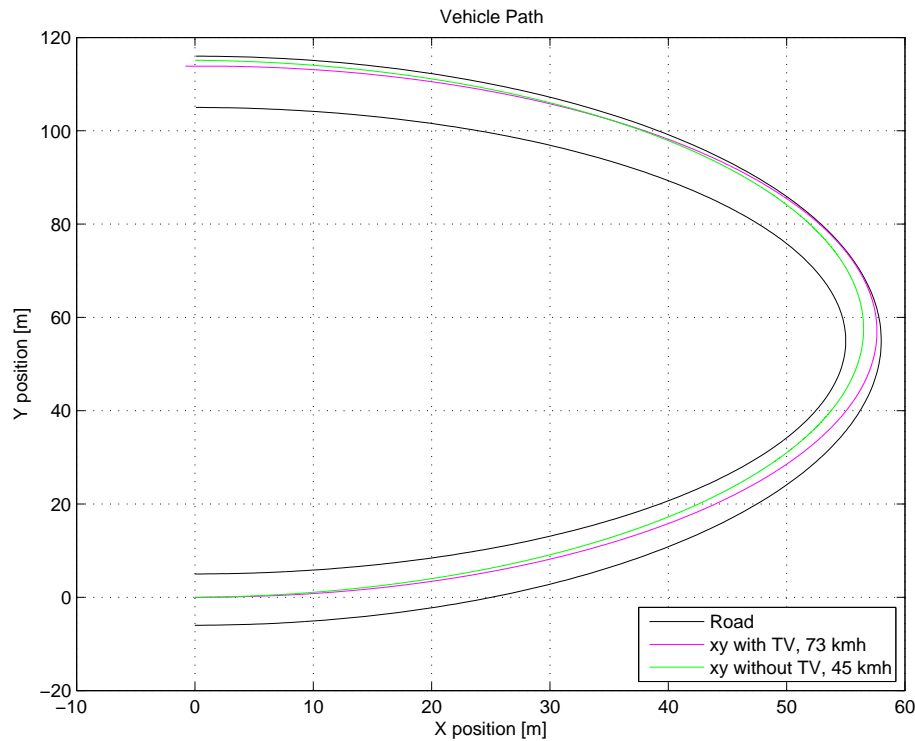


Figure 8-7: Plot of the vehicle paths for a 180° turn

achieve the highest possible velocity without driving outside the corner. In all three runs the steering angle is 30 degrees and the initial velocity is equal to the exit velocity. The throttle is scaled to the velocity and therefore differs for all three runs. In all the runs the buffer capacity is included in the total power of the vehicle, so the vehicle runs on full power.

In Figure 8-7 the simulation results of a fixed corner of 180° is shown. When no torque vectoring is applied the maximum velocity is only 45 km h^{-1} . The path of the vehicle starts in the middle of the road but after the corner diverges to the outer side of the road. For the case with torque vectoring the maximum velocity is 73 km h^{-1} which is significantly higher then when no torque vectoring was applied. The path for torque vectoring is much wider and closer to the outer side of the road then when no torque vectoring was used. This is mainly due to the higher velocity which pushed the vehicle to the outer side.

8-4 Double lane change

In this simulation a double lane change is performed on the vehicle to simulate quick corner behavior. In this test the vehicle will begin with an initial velocity of 100 km h^{-1} without throttle input. During the run the vehicle tries to follow the ideal path through the double lane change. The cornering test is executed 3 times, with and without torque vectoring. In both runs the buffer capacity is included in the total power of the

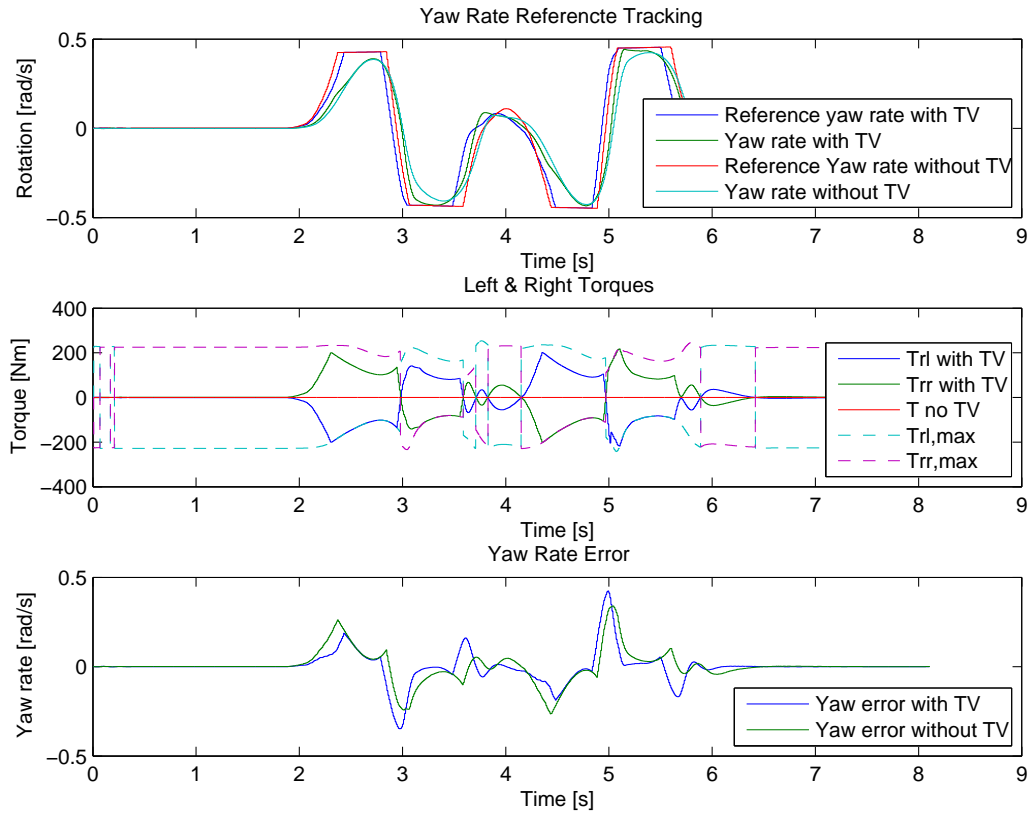


Figure 8-8: Plot of the yaw tracking, controller in/output and torques for a double lane change

vehicle. This means that the vehicle runs on full power for the whole test procedure.

In Figure 8-8 and Figure 8-9 the simulation results of the double lane change are shown. The first run is executed with the vehicle without torque vectoring. In this run the exit velocity is 87.21 km h^{-1} . The run with no torque vectoring has a relatively large overshoot, compared to the runs with torque vectoring, even though the velocity is lower. The second run is with torque vectoring and shows a path with a smaller overshoot, this means that the cornering behavior is improved. The vehicle is now capable of taking a corner with a smaller radius. The second subplot of Figure 8-9 shows the energy consumption of the vehicle during the run. The energy consumption is zero for both with and without torque vectoring. This is due to the total drive torque constraint. Due to this constraint the total drive torque is zero, because the throttle input is zero.

8-5 Conclusion

Looking at the four different test procedures, it is clear that also this torque vectoring control algorithm has an effect on the vehicle's behavior. When torque vectoring is used the lateral behavior of the vehicle improves and leads to higher velocities when corners are taken. This improvement in velocity can lead to faster lap times, as the vehicle will

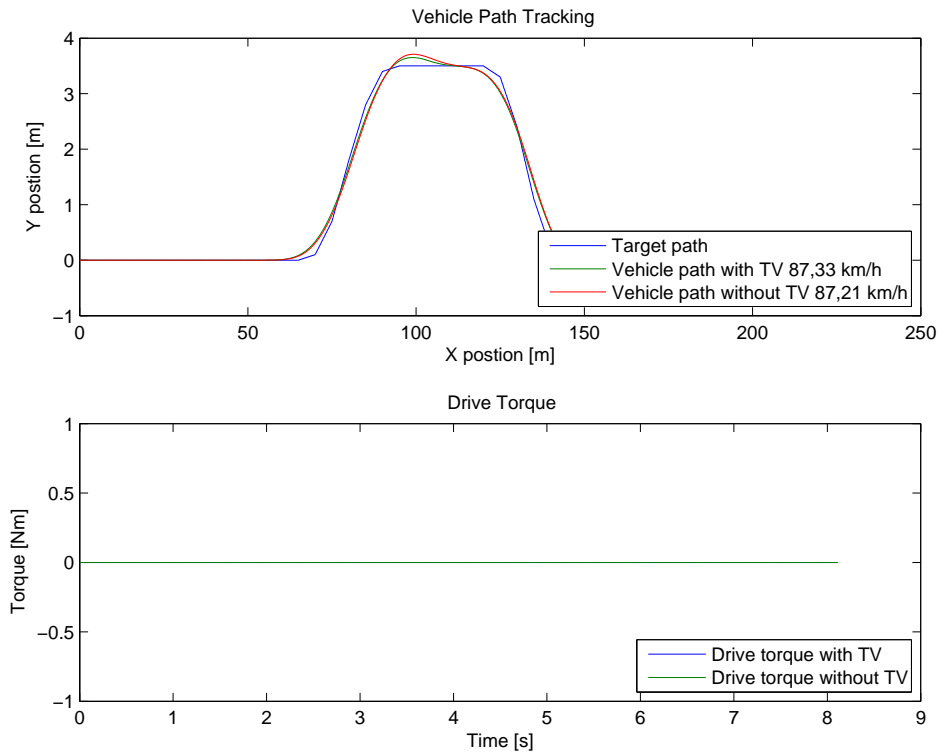


Figure 8-9: Plot of the vehicle path for a double lane change

leave the corner with a higher velocity than when no torque vectoring is applied. Only in the last test procedure, the double lane change, there is no significant difference. The choice of including the total drive torque constraint is the main cause for this insignificant difference. The controller forces the drive torque to be zero, such that no extra energy is consummated. Torque vectoring is in all test procedures capable of driving in a more ideal line. The controller is, when possible, tracking the desired yaw rate. It can then be concluded that with the LP controller the vehicle behaves like a neutral steered vehicle.

Chapter 9

Conclusion

Torque vectoring is in principle a vehicle stability control system, and is mostly used to give the vehicle an ideal balance between ride comfort, response, stability and fuel economy. Torque vectoring can also be used to improve the vehicle performance and still improve both the stability and the response without sacrificing comfort and safety. With this ability to improve the vehicle performance, torque vectoring was chosen to be implemented in the Forze VI. The Forze VI is a hydrogen powered racing vehicle with Rear Wheel Drive (RWD). The two rear wheels are powered by two separate electrical motors. The objective is to construct a torque vectoring algorithm which increases the overall performance for the Forze VI. This control algorithm needs to be designed especially for the Forze VI and must be capable to be used in real-time. Ideally, the control algorithm is adjustable to fulfill the drivers preferences. Torque vectoring should therefore ultimately lead to faster lap times, such that Forze VI will be able to set lap records. The problem statement of this thesis is as follows:

“Constructing a torque vectoring algorithm which ensures better lateral vehicle performance and faster lap times, than when no torque vectoring is used.”

In Chapter 5 the first controller was presented. This controller is a PI controller with an LP to determine the rear wheel torques. The controller was based upon a linear single track model, because of the limited knowledge of the vehicle parameters. Due to the fact that there was little knowledge of the tire parameters, there was chosen for a linear tire model as well. To prevent the wheels from slipping, torque restrictions are opposed. These torque restrictions are determined by the current wheel loads and the tire-road friction coefficient μ_{res} . An PI controller is not capable of handling with constraints, therefore the LP is used to determine the final wheel torques, with respect to all the torque constraints. To determine the final wheel torques two different LP problems are used. One maximizes the torque vectoring torque while ensuring the total drive torque to be equal to the demanded drive torque. This is chosen by setting $\kappa = 0$, $TV(0)$. The

other maximizes the torque vectoring torque without ensuring the total drive torque to be equal to the demanded drive torque. This way the full torque vectoring potential will be used and is chosen by setting $\kappa = 1$, $TV(1)$.

In Chapter 6 the first controller was presented, it was concluded that:

1. Torque vectoring has a positive effect on the vehicle's performance. When torque vectoring is used the lateral behavior of the vehicle improves and leads to higher velocities when corners are taken.
2. The upside of $TV(0)$ is that the drive torque is still proportional to the throttle at all times. The driver will not notice a change in drive torque and therefore $TV(0)$ will have less impact on the drivers experience. This also means that the energy consumption will not increase compared to the non torque vectoring case.
3. The downside of $TV(0)$ is that the vehicle will perform less in quick handling maneuvers and where the smallest corner radius is desired. Not all the torque vectoring potential will be used, because the drive torque constraint prevents this.
4. The Upside of TV with $TV(1)$ is that the torque vectoring potential is fully used. The performance is significantly better in all test procedures, and will lead to the best increase in terms of lap times.
5. The downside of $TV(1)$ is that the driver will notice the decrease or increase in drive torque. The driver is therefore no longer in control over the acceleration or deceleration of the vehicle.
6. The controller is, when the torques are not restricted, tracking the desired yaw rate. It can then be concluded that with both $TV(0)$ and $TV(1)$ the vehicle behaves like a neutral steered vehicle.

In Chapter 7 the second controller was presented. This controller is a combination of the PI controller and LP problem of the first controller. By integrating the PI controller into the LP problem, $TV(LP)$, it is now possible to incorporate the constraints into the controller instead of applying the constraints afterwards. Due to new sensors that became available in the Forze VI, more vehicle parameters could be measured. This gave the opportunity to replace the linear single-track model with a non-linear two-track model. The tire model is also not linear anymore, the friction coefficient is now dependent on the wheel slip and the slip angle. With the controller based upon the non-linear two-track model, the controller is now capable of determining the torques for a All Wheel Drive (AWD) vehicle. The current Forze is still RWD, but when AWD will be implemented, this controller can still be used.

In Chapter 8 the second controller was presented, it was concluded that:

1. $TV(LP)$ has a positive effect on the vehicle's performance. There is a clear increase in the lateral performance compared to the vehicle with no torque vectoring

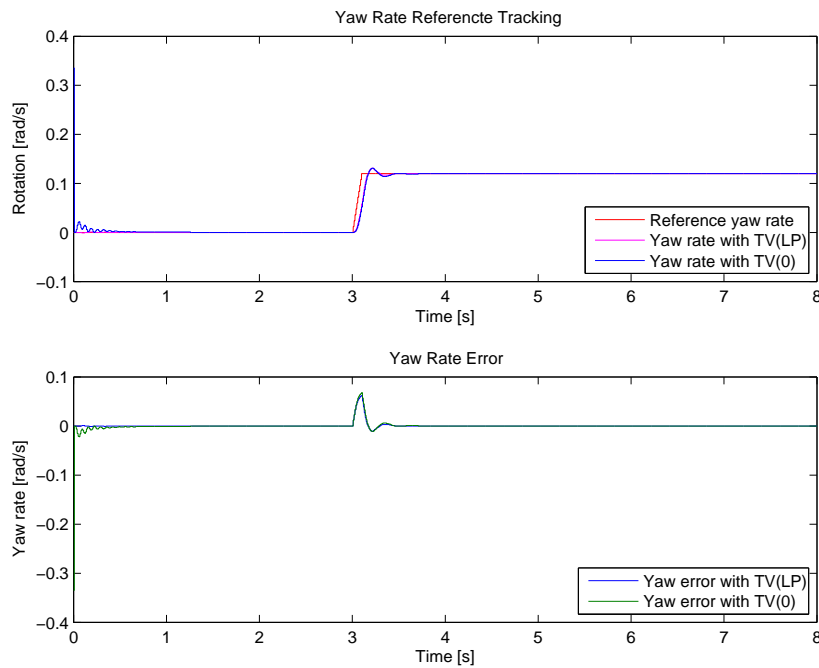


Figure 9-1: Comparison of the yaw rate tracking and controller in/output for a step response of 10°

2. For $TV(LP)$ the drive torque is still proportional to the gas pedal at all times. The driver will not notice a loss in drive torque. The LP controller will therefore have less impact on the driver's experience. This also means that the energy consumption will not increase compared to the non torque vectoring case.
3. For the double lane change there is no significant increase in the exit velocity, but the deviation from the desired line is significant smaller.
4. $TV(LP)$ is, when the torques are not restricted, tracking the desired yaw rate. It can then be concluded that with $TV(LP)$ the vehicle behaves like a neutral steered vehicle.

When the two controller are compared it is clear that the second controller is very similar to the first controller $TV(0)$. This is not strange, both controllers are based upon a PI controller and share the same total drive torque constraint. Both controller can therefore not fully use the torque vectoring potential. The first controller $TV(1)$ does not share that constraint and can use the full torque vectoring potential. This is the reason that the best lateral performance comes from $TV(1)$. But this performance comes at a cost, there is more energy consummated then for the other two controllers. Furthermore the driver does not have full control on the total drive torque, this can decrease or increase without his intention.

Although $TV(0)$ and $TV(LP)$ look very similar they are not identical. This can be explained by the fact that the K_i and K_p values and the used models are different. Looking at the 10 degree step response for both controllers, see Figure ?? and Figure ??,

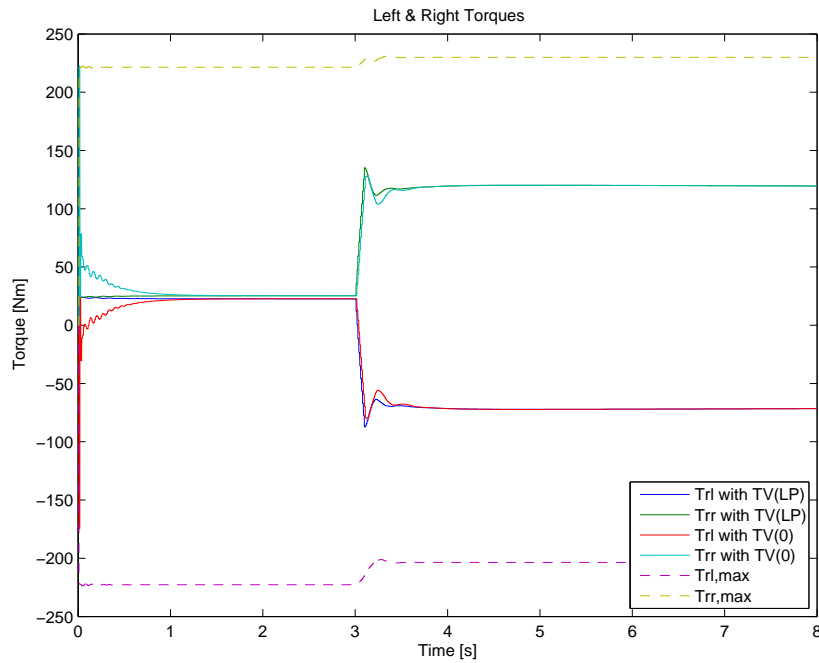


Figure 9-2: Comparison of the yaw rate tracking and controller in/output for a step response of 10°

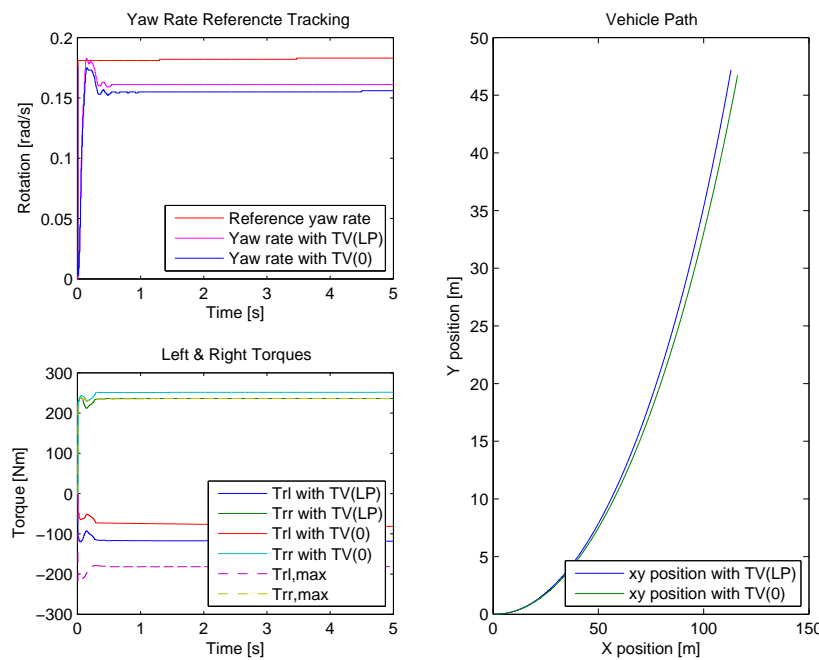


Figure 9-3: Comparison of the yaw rate tracking and controller in/output for a step response of 10°

the overshoot is the same, but the settling time is just a bit better for $\text{TV}(LP)$ then for $\text{TV}(0)$. The settling time is about 0.01 second faster for $\text{TV}(LP)$ then for $\text{TV}(0)$. The torques generated by $\text{TV}(LP)$ rise faster and are sharper then the torques from $\text{TV}(0)$. The control output of $\text{TV}(LP)$ is slightly more aggressive the the control output of $\text{TV}(0)$. This is the reason that $\text{TV}(LP)$ shows better tracking results then $\text{TV}(0)$. For the continues steer input, see Figure ??, $\text{TV}(LP)$ also performs better. $\text{TV}(LP)$ achieves a larger torque vectoring torque then $\text{TV}(0)$ and therefore creates a larger yaw moment. This larger yaw moment leads to a higher yaw rate and therefore better tracking.

$\text{TV}(0)$ does however outperform $\text{TV}(LP)$ in the 180 degree and the double lane change. The expatiation would be that this is the other way around. The previous results showed that $\text{TV}(LP)$ had better overall performance then $\text{TV}(0)$. Both exit velocities are lower for $\text{TV}(LP)$ then for $\text{TV}(0)$. It seems that $\text{TV}(LP)$ shows better performance in the yaw rate tracking than $\text{TV}(0)$, but at the cost of the velocity. The maximum longitudinal forces of $\text{TV}(LP)$ are smaller then $\text{TV}(0)$ in all four test procedures. This means that the total drive torque is lower. The lower drive torque will be the main reason the exit velocities are lower. This is also confirmed in the double lane change. The exit velocity of $\text{TV}(0)$ is 87.39 km h^{-1} against 87.21 km h^{-1} of $\text{TV}(LP)$.

$\text{TV}(LP)$ uses a non-linear vehicle model and a non-linear tire model instead of a linear single-track and linear tire model. It could be possible that the added complexity to the model causes a larger mismatch between the modeled vehicle dynamics and the actual vehicle dynamics. It is therefore possible that the non-linear model does not correctly estimate the maximum longitudinal forces or the lateral forces. If the maximum longitudinal forces would be better estimated, the performance of $\text{TV}(LP)$ could be increased. It would therefore be a recommendation to research for different non-linear methods to determine the lateral and maximum longitudinal forces.

Chapter 10

Future Work Proposals

10-1 More detailed modeling

In this thesis multiple models are presented. Most models suffice for there purpose, but other models could be improved. In this section several future models are proposed. These are considered likely to improve the controller performance and accuracy.

10-1-1 Tire model

In this thesis, the Burckhard method is used to determine the lateral friction force of the tires. This method uses only one curve to describe the friction coefficient based on the slip ratios. The lateral forces are then calculated by multiplying the friction coefficient with the wheel loads. This model of the friction coefficient gives a relative accurate value of the friction without having much knowledge of the tire. This simplified model does not consider any dynamic effects. When more knowledge of the tire is available, or even Pajecka parameter, more elaborate tire models can be considered. Some semi-empirical models that could be chosen are Dugoff's tire model [2] or the magic tire formula of Pajecka [11]. These models have in common that there are well capable of capture the dynamic behavior of the tires. These models will therefore give more accurate lateral wheel forces. The improvement of the accuracy of the lateral wheel forces will directly improve the control, because the model accuracy increases.

10-1-2 Steering model

In this thesis, the steering angle δ is determined with the use of a model based upon the steering mechanics and an estimated model of the dynamic toe. There is a model for the dynamic toe of the front and the rear and it is not empirical. Because the models are not empirical, it this means that when mechanical changes occur in the vehicle this

estimated model will no longer be valid. It is therefore recommended to determine an empirical model such that mechanical changes can be directly imported into the model.

10-2 Tire-Road friction model

The Burckhard model used in this thesis is a static curve based on the known tire parameters. These parameters are based upon a standard asphalt road. In practice the friction coefficient for each asphalt road is different, so there will always be a deviation between the assumed tire-road friction coefficient and the actual tire-road friction coefficient. Furthermore there is assumed that the tire-road friction coefficient is constant during the whole race, but the tire-road friction coefficient in reality differs over the whole race. This is due to the change in temperature of the road and the tires, which caused the tire-road friction coefficient to change. The wear of the tire is also playing an important role in the change of the tire-road friction coefficient. It is therefore recommended that a tire-road friction estimation model is used along with a more comprehensive tire model. This should allow the controller to produce more accurate torques.

10-3 More comprehensive simulations

10-3-1 Circuit simulation

The simulation shown in Section 6, shows mostly handling maneuvers for step steer inputs, turns and double lane changes. These simulations show the increase in speed and therefore the possibility in faster lap-time. As these simulations predict faster lap-times, there is no clear answer how much the vehicle will be faster in one lap. With a circuit simulation this actual difference in lap-time could be simulated. With a circuit simulation the values of κ and α can be chosen so that it produces the fastest lap-times. Because circuits are all different, each circuit simulation can help to optimize the controller to produce the fastest lap-time for each circuit.

10-3-2 Real-time simulation

In Chapter 6 most simulations are not real-time. In the case of non real-time simulations, the linear control problem can solve the problem as it has always enough time. In Section 6 there is one real-time simulation showing a lap around Zandvoort. This real-time simulation is performed on two computers, one computer running CarSim and LabVIEW and the other computer running the visualization. The simulation computer has different hardware than the hardware of the computer that will be used in the Forze VI. It is therefore important to test the simulation with the hardware of the Forze VI, before it can be tested in the Forze VI in real-time.

10-4 Pre-processor

The pre-processor presented in Section 5, generates a desired yaw rate $\dot{\psi}_{des}$ based upon a under-steer gradient of zero $K_U = 0$. The under-steer gradient is static, so for each corner the desired yaw rate is determined with an under-steer gradient of zero. When the under-steer gradient is zero, the vehicle has equal slip angles at the front and the rear. By changing the under-steer gradient, this ratio changes. Changing the under-steer gradient therefore means changing the cornering behavior. The under-steer gradient is now chosen to be static trough a corner, but it can also be variable. It could be a possibility to enter the corner with over-steer gradient and exit with under-steer gradient. However, additional research is needed whether a changing under-steer gradient, can improve the cornering behavior compared to a static under-steer gradient.

10-5 Suspension jounce measurements

In Section 5-3-1 the wheel loads are determined with the use of a geometrical approach. This approach is depended on a lot of different vehicle parameters. In this thesis, these vehicle parameters values are from the initial designed vehicle model. These values are not yet confirmed with the actual vehicle and confirming all these parameter values is very cumbersome. A less cumbersome possibility can be to determine the wheel loads by measuring the suspension jounce. This suspension jounce could then be used to determine the wheel loads, with the use of the relation between the jounce and the suspension constant. This method will also not be effected by all the changes made in the stiffness of the body. However, additional research is needed if these special suspension sensors are suitable for the Forze VI.

10-6 Noise testing

In all the simulations in Chapters 6 and 8 the input signals are noise free. The simulations therefore show only the result for an ideal situation. It would therefore be a recommendation to test both controllers with noise. This will give a more accurate view of the controllers behavior in real-time.

Bibliography

- [1] K. Sawase and Y. Ushiroda, "Improvement of vehicle dynamics by right-and-left torque vectoring system in various drivetrains," tech. rep., *Mitsubishi motors*, 2008 no. 20.
- [2] R. Rajamani, *Vehicle Dynamics and Control*. Mechanical Engineering Series, Springer Verlag, 2006.
- [3] T. Schuit, "Vehicle dynamics a." Assignments and documentation for WB3404A and ME1460-3, June 2014.
- [4] W. F. Milliken and D. L. Milliken, *Race car vehicle dynamics*. Warrendale, PA, U.S.A.: SAE International, 1995. 94036941 William F. Milliken, Douglas L. Milliken. ill. ; 26 cm. Includes bibliographical references (p. [841]-854) and index.
- [5] M. Klomp, *Longitudinal Force Distribution and Road Vehicle Handling*. 2010.
- [6] F. Bottiglione, A. Sorniotti, and L. Shead, "The effect of half-shaft torsion dynamics on the performance of a traction control system for electric vehicles," *Proceedings of the Institution of Mechanical Engineers, Part D: Journal of Automobile Engineering*, 2012.
- [7] U. Kiencke and L. Nielsen, *Automotive Control Systems*. Berlin, Heidelberg: Springer Berlin Heidelberg, 2005.
- [8] H. Pacejka, *Tyre And Vehicle Dynamics*. Automotive engineering, Butterworth-Heinemann, 2006.
- [9] M. Burckhardt, *Fahrwerktechnik: Radschlupf-Regelsysteme*. Vogel FachBuch, Würzburg, 1993.
- [10] M. M and H. Wallentowitz, *Dynamik der Kraftfahrzeuge*, vol. Edition 4. Springer Verlag, Berlin, 2004.

-
- [11] H. B. Pacejka and E. Bakker, “The magic formula tyre model,” *Vehicle System Dynamics*, vol. 21, no. sup001, pp. 1–18, 1992.

Glossary

List of Acronyms

TU Delft	Delft University of Technology
ESP	Electronic Stability Program
ABS	Anti-lock Braking System
AWD	All Wheel Drive
RWD	Rear Wheel Drive
CoG	Center of Gravity
ICM	Instantaneous Center of Motion
PID	Proportional Integral Derivative
PI	Proportional Integral
SAE	Society of Automotive Engineers
GPS	Global Positioning System
IMU	Inertial Measurement Unit
ICM	Instantaneous Center of Motion
LP	Linear Programming
MCS	Mobile Control Systems
TV	Torque Vectoring

List of Symbols

Greek Symbols

Symbol	Units	Description
α		Torque vectoring performance weight
α_{ij}	[rad]	Slip angle
β	[rad]	Sideslip angle
$\ddot{\psi}$	[rad s ⁻²]	Yaw acceleration
δ_{ij}	[rad]	Steering angle
ΔR_{ij}	[m]	The differential radii
$\dot{\beta}$	[rad s ⁻¹]	Sideslip angle rate
$\dot{\psi}$	[rad s ⁻¹]	Yaw rate
$\dot{\psi}_{des}$	[rad s ⁻¹]	Desired yaw rate
$\dot{\psi}_{max}$	[rad s ⁻¹]	Upper bound yaw rate
$\dot{\psi}_{ref}$	[rad s ⁻¹]	Reference yaw rate
$\tilde{\dot{\psi}}$	[rad s ⁻¹]	Yaw rate error
ℓ	[m]	Wheelbase
ℓ_f	[m]	Wheelbase front
ℓ_r	[m]	Wheelbase rear
ϵ		exact penalty function
κ		Torque vectoring performance factor
$\lambda_{max,ij}$		Maximum allowable slip-ratio
μ		Tire-road coefficient
$\mu_{l,ij}$	[m s ⁻¹]	Longitudinal friction coefficient
$\mu_{r,ij}$	[m s ⁻¹]	Resultant friction coefficient
$\mu_{s,ij}$	[m s ⁻¹]	Lateral friction coefficient
σ		Contribution factor
v_x	[m s ⁻¹]	Longitudinal velocity
v_y	[m s ⁻¹]	Lateral velocity
v_{CoG}	[m s ⁻¹]	Velocity at CoG
v_{ctrl}	[rad s ⁻¹]	Vehicle control set-point velocity
$v_{R,ij}$	[m s ⁻¹]	Rotational equivalent wheel velocity
$v_{W,ij}$	[m s ⁻¹]	Wheel velocity

Roman Symbols

Symbol	Units	Description
$\bar{F}_{l,ij}$	[N]	Maximum longitudinal friction force
$\bar{F}_{s,ij}$	[N]	Maximum lateral friction force
$\bar{F}_{wl,ij}$	[N]	Maximum longitudinal wheel friction force
$\bar{F}_{x,ij}$	[N]	Maximum longitudinal force

\vec{F}_{sv}	[N]	Slack variable
A	[m ²]	Reference frontal area
a_x	[m s ⁻²]	Longitudinal acceleration
A_Y		Lateral acceleration in g units
a_y	[m s ⁻²]	Lateral acceleration
C_f	[N rad ⁻¹]	Cornering stiffness front
C_r	[N rad ⁻¹]	Cornering stiffness rear
C_{ij}	[N rad ⁻¹]	Cornering stiffness
$C_{l,i}$		Lift coefficient
C_{rm}		Roll moment coefficient
$F_{l,ij}$	[m s ⁻¹]	Longitudinal friction force
$F_{s,ij}$	[m s ⁻¹]	Lateral friction force
F_{tot}	[N]	Total demanded torque
$F_{wl,ij}$	[m s ⁻¹]	Longitudinal wheel friction force
$F_{ws,ij}$	[m s ⁻¹]	Lateral wheel friction force
$F_{x,ij}$	[N]	Longitudinal tire force
$F_{y,ij}$	[N]	Lateral tire force
g	[m s ⁻²]	Gravitational acceleration
G_r		Gear ratio
H	[m]	Distance CoG to roll axis
h	[m]	CoG height
J_z	[kg s ⁻²]	Inertia moment
K_u		Under-steer gradient
$K_{rf,A}$	[N m rad ⁻¹]	Front ARB stiffness
K_{rf}	[N m rad ⁻¹]	Roll stiffness of the front
$K_{rr,A}$	[N m rad ⁻¹]	Rear ARB stiffness
K_{rr}	[N m rad ⁻¹]	Roll stiffness of the rear
K_{wf}	[N m ⁻¹]	Front wheel rate
K_{wr}	[N m ⁻¹]	Rear wheel rate
LF	[N]	Lift force front
LR	[N]	Lift force rear
m	[N]	Vehicle mass
m_f	[N]	mass of the front
m_r	[N]	mass of the rear
M_z	[N m]	Yaw moment
q	[kg m ⁻²]	Dynamic pressure
R	[m]	Circular road radius
$r_{eff,f}$	[m]	Effective tire radius front tire
$r_{eff,r}$	[m]	Effective tire radius rear tire

Rm	[N m]	Roll moment
s_f	[m]	Half track width front
s_r	[m]	Half track width rear
$s_{l,ij}$		Longitudinal slip coefficient
$s_{r,ij}$		Resultant slip coefficient
$s_{s,ij}$		Lateral slip coefficient
T_{ij}	[N m]	Wheel torque
$T_{max,ij}$	[N m]	maximum torque
T_{max}	[N m]	maximum motor torque
$T_{max}(\omega)$	[N m]	motor torque limit
$TV_{control}$	[N m]	Demanded torque vectoring torque
W_F	[N]	Wheel load front
W_R	[N]	Wheel load rear
$W_{ab,ij}$	[N]	Anti-roll bar load
$W_{aero,ij}$	[N]	Aerodynamic load
W_{ij}	[N]	Wheel load
$W_{s,ij}$	[N]	Static Wheel load
$W_{x,ij}$	[N]	Longitudinal load
$W_{y,ij}$	[N]	Lateral load

Subscripts

Symbol	Units	Description
fl		Front left tire
fr		Front right tire
rl		Rear left tire
rr		Rear right tire